Journal of Nanobiotechnology

RESEARCH

Open Access

A multiple-crosslinked injectable hydrogel for modulating tissue microenvironment and accelerating infected diabetic wound repair

Zhengduo Zhang[1†], Yuanyuan Ding[2†], Huipu Yuan[2], Chen Rui[2], Pengfei Fan[1], Yinwen Ji[2], Ying Xiao[2*], Jiayong Dai[2*] and Lei Li[1*]

Abstract

Elevated oxidative stress and inflammation, bacterial infections, and vascular impairment undoubtedly impede the normal diabetic wound healing process, which has encouraged the development of high-performance dressings for wound management. Herein, a new type of multiple-crosslinked injectable hydrogel, GCP, was developed via the radical polymerization of propenyl groups and the formation of copper–polyphenol coordination bonds and Schiff base bonds. The copper–polyphenol coordination and Schiff base bonds in the GCP hydrogel were disrupted in the acidic microenvironment of diabetic wound, resulting in the release of copper ions and protocatechualdehyde (PA) to scavenge reactive oxygen species (ROS), promote angiogenesis and cell migration, and exert antibacterial and anti-inflammatory activities via the CuPA complexes. Consequently, markedly accelerated infected diabetic wounds healing was achieved through this tissue microenvironment remodeling strategy. Moreover, the underlying mechanism of the antibacterial properties was investigated by 16S rRNA sequencing. The results indicated that the CuPA complexes can clearly inhibit the growth and reproduction of *S. aureus* by downregulating specific genes associated with ABC transporters, hindering bacterial protein synthesis, and enhancing oxidoreductase activity. This innovative hydrogel platform for wound management may inspire new methods for the preparation of high-performance biomedical materials and the treatment of other clinical diseases.

Keywords Multifunctional hydrogel, Metal–polyphenol complex, Microenvironment responsive, Macrophage repolarization, Infected diabetic wound

†Zhengduo Zhang and Yuanyuan Ding contribute equally to this paper.

*Correspondence:
Ying Xiao
xiaoying.srr@zju.edu.cn
Jiayong Dai
daijy@zju.edu.cn
Lei Li
lilei@njmu.edu.cn

Graphical Abstract

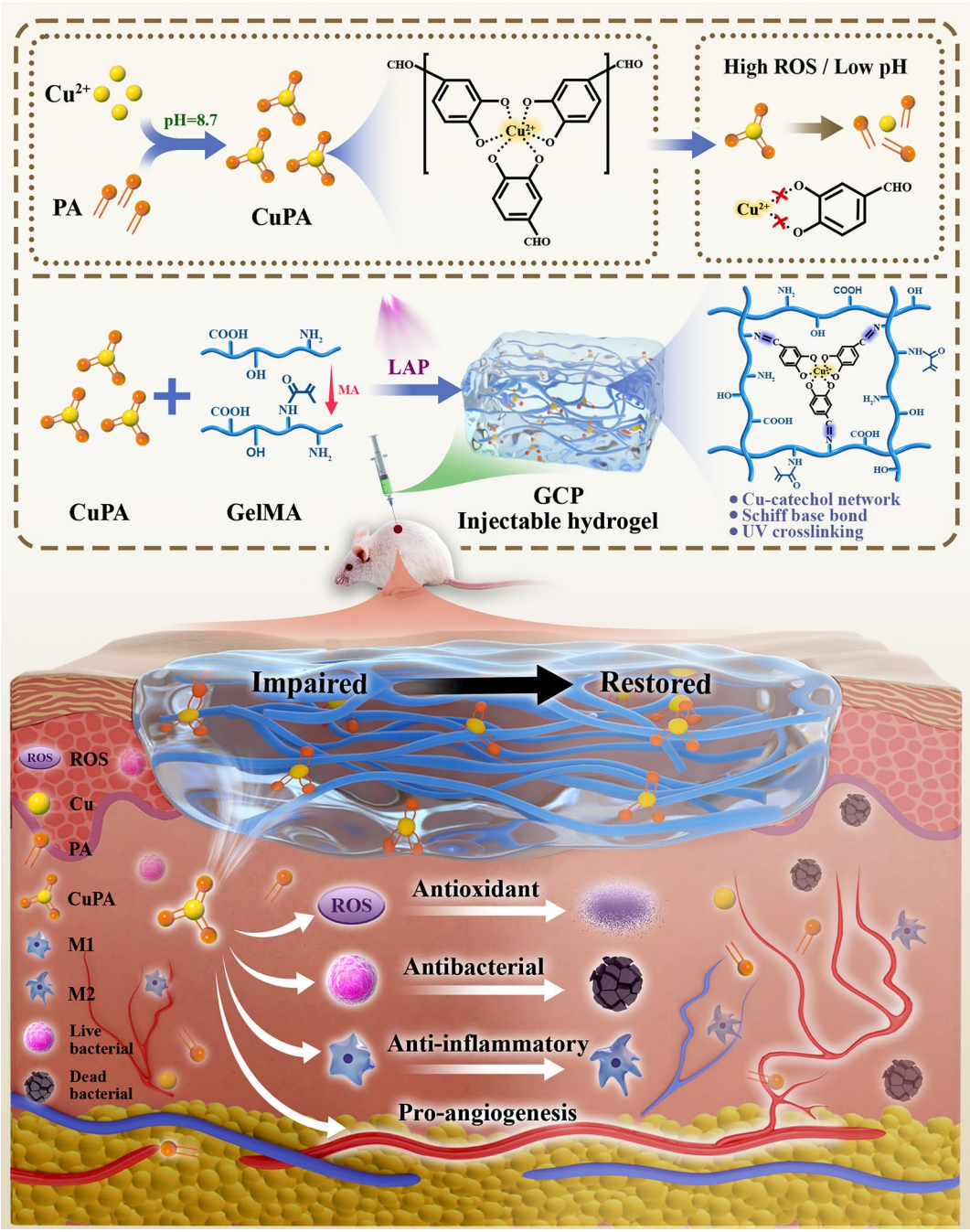

Introduction

As the global population continues to age, the incidence and prevalence of age-related chronic diseases, such as diabetes, are increasing each year and are projected to reach 1.31 billion by 2050 [1], which not only causes discomfort and inconvenience for patients but also escalates the financial burden on families and the broader society. Individuals with diabetes commonly exhibited dysregulated carbohydrate, lipid, and protein metabolism [2], resulting in impaired protein synthesis and tissue regeneration, weakened immune function and delayed wound healing. Consequently, diabetic wounds are among the most severe chronic complications faced by diabetic patients. Unfortunately, in addition to the elevated glucose levels and oxidative stress within the

wound microenvironment that severely impede the natural healing process, recurrent bacterial infections also transform acute wounds into chronic refractory conditions [3], notably extending the duration of wound repair and exacerbating patient discomfort. Therefore, developing high-performance dressings aimed at enhancing the recovery of infected diabetic wounds holds great clinical significance and social value.

The spontaneous healing of skin injuries commonly encompasses four overlapping phases, hemostasis, inflammation, proliferation, and tissue remodeling [4], and represents a highly complex biological process involving spatiotemporal and orderly interactions among various cells [5], extracellular matrix components [6], and cytokines [7], restoring the skin barrier and maintaining tissue homeostasis. Dysregulation in one or more of these stages may lead to the formation of chronic, unhealed wounds or pathological scars. Owing to impairments in peripheral circulation, platelets and fibrinogen, which serve as crucial cellular and stromal constituents involved in the hemostatic phase of wound healing [8], these factors are unable to reach the hemorrhagic site promptly to perform their function. In addition, the inadequate supply of oxygen and nutrients essential for tissue regeneration prevents local necrotic materials from being removed in a timely manner [9], which may trigger infection. Furthermore, immune cells, particularly neutrophils and macrophages, rapidly infiltrate wounds and secrete many chemokines and cytokines to recruit cells and promote cellular proliferation [10]. These immune cells also efficiently release various proteases and generate reactive oxygen species (ROS) to counteract the invasion of pathogenic microorganisms and remove damaged cells [11]. Although early inflammatory responses facilitate wound recovery, extensive research has shown that the sustained presence of increased levels of immune cells or prolonged inflammation can compromise cellular structure and function, contributing to dysregulated repair mechanisms and delayed wound healing [12]. This intricate condition of infected diabetic wounds places stringent demands on advanced dressings designed to improve the wound healing microenvironment.

Hydrogels, which are characterized by a high moisture content (80–90%) and a three-dimensional network structure, closely mimic natural tissue and demonstrate superior abilities to absorb tissue exudates, retain moisture, and facilitate gas exchange and are anticipated to address the challenges mentioned above [13]. Gelatin methacryloyl (GelMA) contains extracellular matrix (ECM) components and is widely recognized for its excellent tissue adhesion, hemostatic capabilities, and biocompatibility. However, its limited functionality restricts its ability to effectively address the challenges posed by complex wounds. Therefore, GelMA can be appropriately functionalized by incorporating cytokines, drug molecules, nanomaterials, or stem cells, and subsequently foster a more favorable local environment for tissue repair by the conditional responsive release of these factors [13, 14]. Among these functional components, metal-phenolic networks (MPNs) stand out as an excellent choice. By integrating suitable metals and polyphenols, MPNs exhibit a variety of enzymatic activities under certain conditions, enabling the elimination of excess ROS in cells and tissues [15], in addition to its antibacterial, anti-inflammatory, pro-angiogenic and immunoregulatory activities. Previous studies by our group and other researchers have proven that copper ions (Cu^{2+}) can inhibit and eradicate pathogenic microorganisms, including *Staphylococcus aureus* (*S. aureus*), *Escherichia coli* (*E. coli*) [16], and *Klebsiella pneumoniae* (*K. pneumoniae*) [17], by interacting with sulfhydryl groups [18], altering bacterial cell membrane permeability, and generating of ROS [19]. Cu^{2+} can also increase the expression of vascular endothelial growth factor (VEGF) and promote collagen synthesis and angiogenesis [20]. Moreover, as an essential trace element in the human physiology, copper possesses a tightly regulated metabolic mechanism and a lower toxicity risk [21]. Polyphenolic compounds, such as tannic acid (TA) and protocatechualdehyde (PA), have been proven to have many pharmacological effects, such as antioxidant, antiapoptotic, and are also able to induce M1 to M2 macrophages polarization during the middle to late stages of tissue regeneration, thereby creating an anti-inflammatory immune microenvironment [22].

Inspired by these data, a new type of multiple-crosslinked injectable hydrogel, GCP, was developed by blending GelMA and copper–protocatechualdehyde (CuPA) networks followed by ultraviolet (UV) irradiation in the presence of lithium phenyl-2,4,6-trimethylbenzoylphosphinate (LAP), where the propenyl groups in GelMA polymerize, copper–catechol coordination occurs, and Schiff base bonds between the amino groups in GelMA and the aldehyde groups in CuPA form. In previous studies, the polyphenols used to form MPNs with copper are primarily TA [23, 24]. Notably, we are the first to combine Cu^{2+} with PA to construct a CuPA network for diabetic wound treatment, aiming to fully exploit the aldehyde groups of the PA to form Schiff base bonds and the hydroxyl groups to establish Cu–catechol coordination, thereby maximizing the mechanical properties of the GCP hydrogel without introducing additional functional modifications. GelMA can facilitate cell adhesion due to its RGD sequence [25] and adhere to skin tissue through hydrogen bonding and π–π stacking interactions, endowing the GCP hydrogel with excellent adhesion performance. Then, the elevated oxidative stress

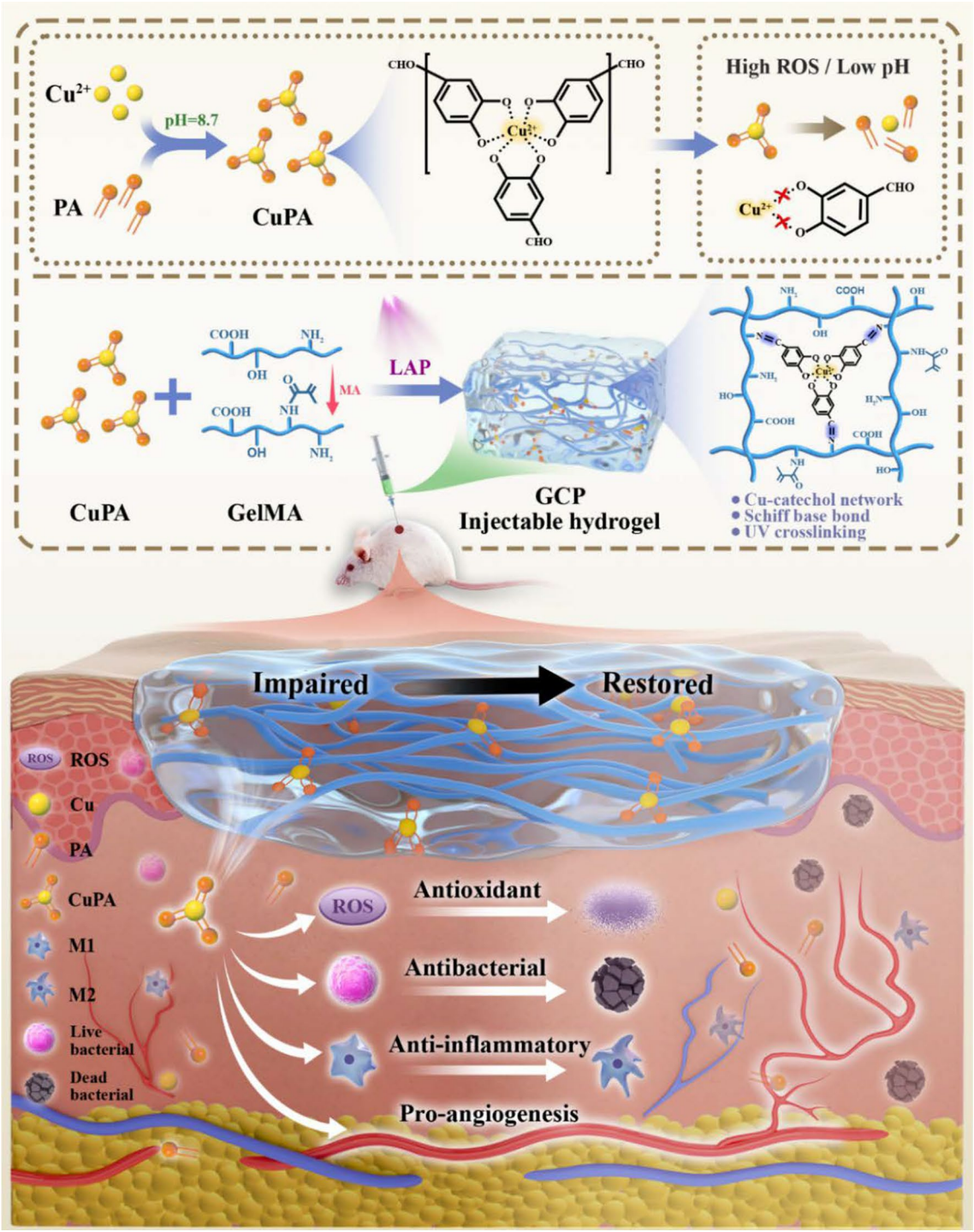

Scheme 1 Schematic representation of the synthesis of the GCP hydrogel and its mechanism in accelerating infected diabetic wound repair. Cu: copper; PA: protocatechualdehyde; ROS: reactive oxygen species; MA: methacrylic anhydride; LAP: lithium phenyl-2,4,6-trimethylbenzoylphosphinate; GelMA: gelatin methacryloyl; M1/M2: M1/M2-polarized macrophages

and reduced pH in the wound microenvironment disrupts the Cu–catechol coordination and the Schiff base bonds, and Cu^{2+} and PA are released into the wound site to regulate different biological processes. The results showed that the GCP hydrogel can reshape the infected diabetic wound environment through its antibacterial,

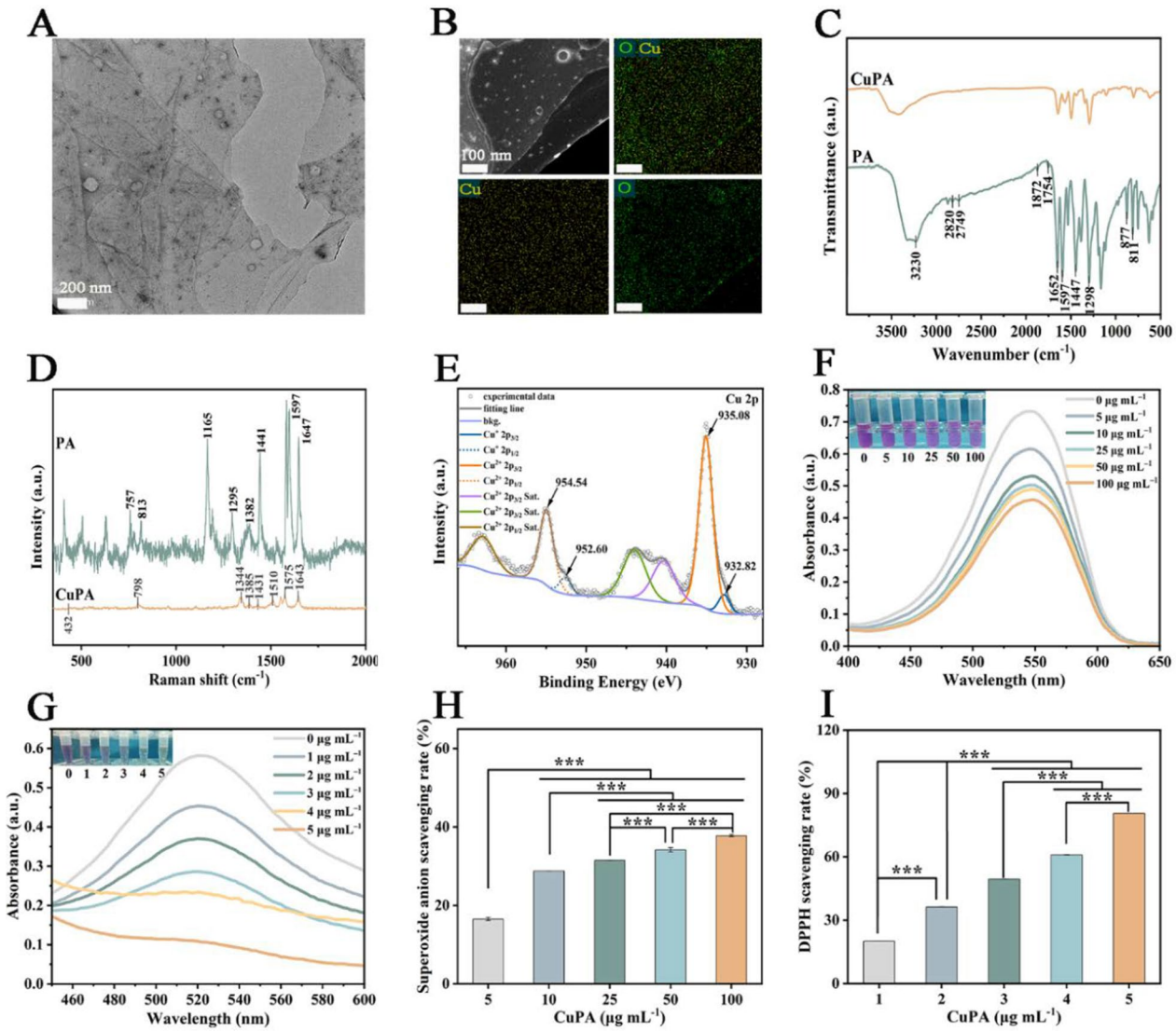

Fig. 1 Characterization and antioxidation properties of CuPA complexes. **A** TEM image of CuPA (scale bar: 200 nm). **B** Elemental mapping of CuPA (scale bar: 100 nm). **C** FTIR spectra of CuPA. **D** Raman spectra of CuPA. **E** XPS spectra of Cu 2p. **F**, **H** Superoxide anion scavenging capacity of CuPA at concentrations ranging from 5 to 100 μg mL^{-1}. **G**, **I** DPPH radical scavenging capacity of CuPA at concentrations of 1–5 μg mL^{-1}. n = 3, mean ± SD, ***p* < 0.05, ****p* < 0.01, *****p* < 0.001

antioxidant, pro-angiogenic, and immunomodulatory effects, consequently enhancing infected diabetic wound repair. Moreover, we fabricated a single network hydrogel (GC) composed of photo-crosslinked GelMA containing ceria nanoparticles (Ce NPs) for comparison because Ce NPs can effectively eliminate ROS in conditions linked to oxidative stress, such as acute kidney injury, ischemic stroke, and diabetic wounds [26–28], on the basis of the interconversion between Ce^{3+} (reduced state) and Ce^{4+} (oxidized state) [29], attenuate the release of inflammatory mediators and suppress the inflammatory response [30]. Compared with those of the GC hydrogel, the antibacterial, angiogenic, and cell migration-promoting capabilities of the GCP were greater. This work is expected to provide novel materials and strategies for the clinical management of infected diabetic wounds. A schematic representation of the above is provided in Scheme 1.

Results and discussion

Synthesis and characterization of the CuPA complexes

CuPA complexes were synthesized by combining $CuCl_2{\cdot}2H_2O$ and PA at a molar ratio of 1: 2, where the catechol moieties on PA chelated to copper ions to

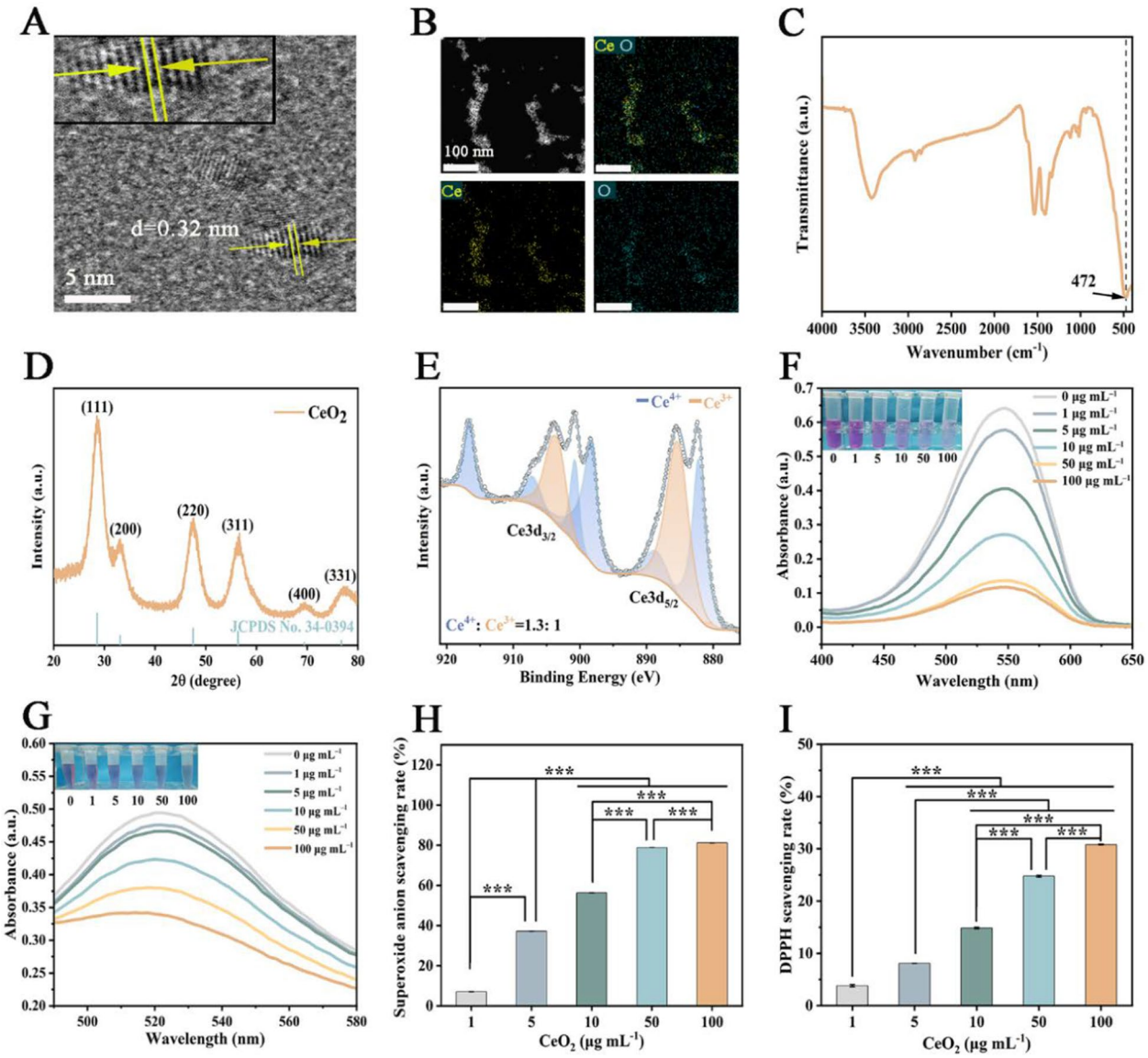

Fig. 2 Characterization and antioxidation properties of Ce NPs. **A** TEM image of Ce NPs (scale bar: 5 nm). **B** Elemental mapping of Ce NPs (scale bar: 100 nm). **C** FTIR spectra of Ce NPs. **D** XRD pattern of Ce NPs. **E** XPS spectra of Ce 3d. **F**, **H** Superoxide anion scavenging capacity of Ce NPs at concentrations ranging from 1 to 100 μg mL^{-1}. **G**, **I** DPPH radical scavenging capacity of Ce NPs at concentrations of 1–100 μg mL^{-1}. n = 3, mean ± SD, ***p* < 0.05, ****p* < 0.01, *****p* < 0.001

establish an MPN. The pH of the reaction was adjusted to 8.7, which mitigates the autooxidation of catechol to quinone while enhancing copper chelation [31]. Transmission electron microscopy (TEM) and elemental mapping analysis revealed that CuPA exhibited a classic sheet structure, with copper evenly distributed throughout the system (Fig. 1A, B). The maximum UV absorption peak of CuPA was observed at 354 nm (Figure S1A, Supporting Information). The characteristic Fourier transform infrared (FTIR) spectroscopy peaks of PA were located at 1872, 1754, 877, and 811 cm^{-1}, indicating the presence of 1,2,4-trisubstituted benzene, whereas the peaks at 1597 and 1447 cm^{-1} were attributed to vibration of the benzene skeleton. The peaks at 3230 and 1298 cm^{-1} were attributed to the stretching vibrations of the C–O and O–H bonds, respectively. The split peaks of the C–H bond in the aldehyde group were detected at 2820 and 2749 cm^{-1} because of Fermi resonance. Moreover, since conjugation with benzene occurs, the stretching vibration peak of the C=O bond in the aldehyde group shifted to a lower frequency of 1652 cm^{-1}. The formation of Cu–catechol coordination bonds in the CuPA complexes

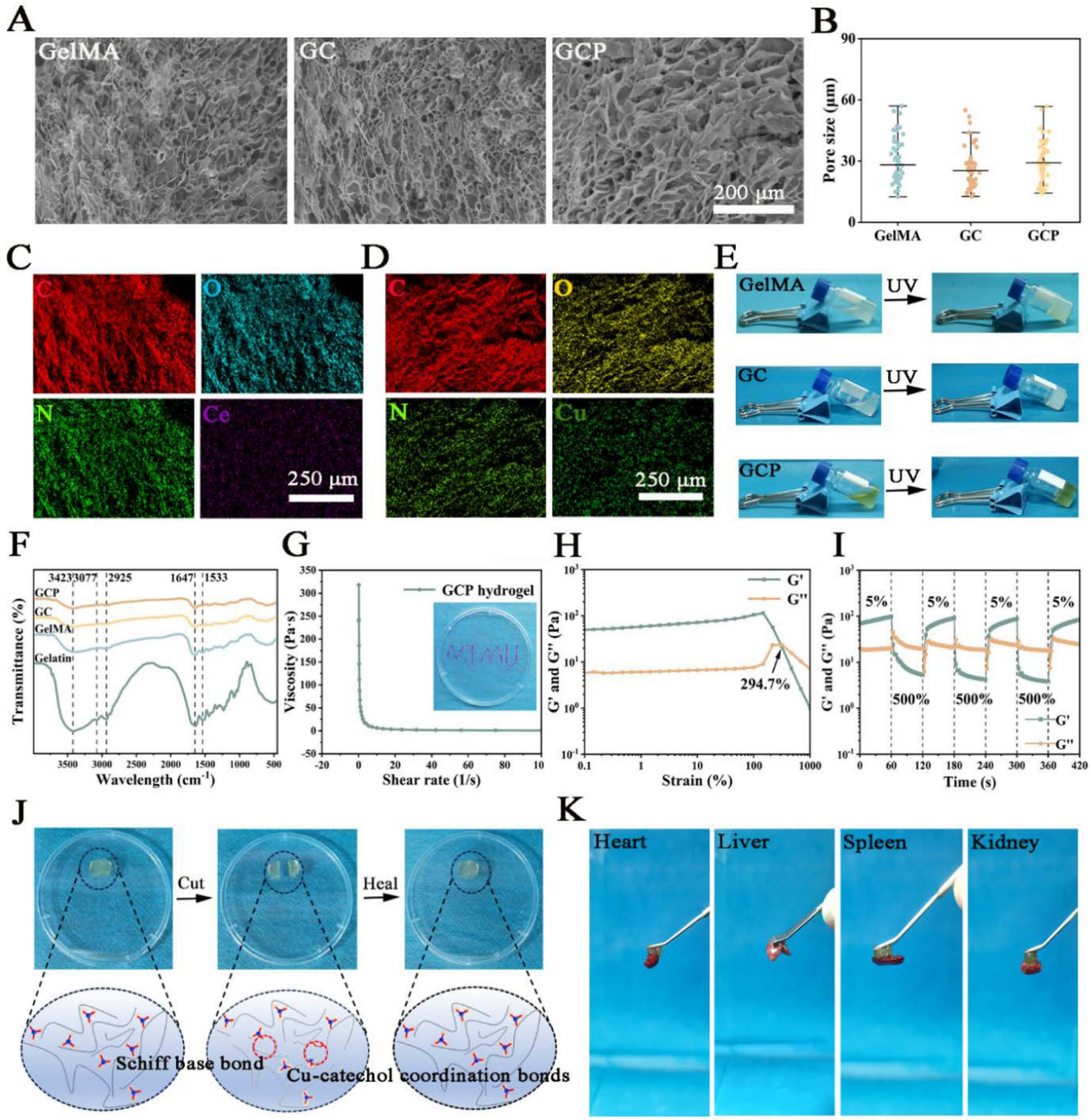

Fig. 3 Characterization of hydrogels. **A** SEM images of GelMA, GC, and GCP hydrogels (scale bar: 200 μm). **B** Quantitative analysis of pore size in various hydrogels (n = 50). **C** Elemental mapping of GC hydrogel and **D** GCP hydrogels (scale bar: 250 μm). **E** Images of GelMA, GC, and GCP hydrogels formation under UV irradiation (395 nm, 3 min). **F** FTIR spectra of gelatin, GelMA, GC, and GCP. **G** Shear-thinning behavior and injectability of GCP hydrogel. **H** Strain amplitude sweeps tests of GCP hydrogel (0.1% to 1000% strain at 1 Hz). **I** Cyclic strain recovery trials of GCP hydrogel across three cycles (5% to 500% strain at 1 Hz). **J** Self-healing properties of the GCP hydrogel. **K** Adhesion capacity of the GCP hydrogel on biological tissues from C57BL/6 mice

resulted in a decrease in peak intensity and a shift toward higher frequencies for PA in general, which may be associated with changes in the molecular structure (Fig. 1C).

The representative Raman peaks of PA in the range of 300–2000 cm^{-1} are showed in Fig. 1D. The peak at 757 cm^{-1} was attributed to the shear vibration of the C–H bond connected to benzene, whereas the peaks at 813

and 1597 cm^{-1} represented the strong stretching vibrations of benzene. The peak at 1165 cm^{-1} was attributed to the vibration of the C–H bond connected to the benzene group and the O–H bond shear vibration. Furthermore, the peak at 1441 cm^{-1} was attributed to the H–C=O shear vibration and partial OH shear vibration, whereas the peak at 1647 cm^{-1} represented the stretching vibration of the C–C=O bond linked to the benzene. Upon the addition of $CuCl_2$, a small peak appeared at 432 cm^{-1}, which is typical of copper chloride. In addition, the characteristic peaks of CuPA shifted in relation to those of PA; for example, the peaks at 813 and 1597 cm^{-1} in the PA spectrum showed displacements of 15 and 22 cm^{-1}, resulting in shifts of 798 and 1575 cm^{-1} in the CuPA spectrum, respectively. Moreover, several peaks were undetectable in the CuPA spectrum and are likely too weak to be distinguished from the background.

The X-ray photoelectron spectroscopy (XPS) data revealed that the peaks attributed to Cu^{+} 2p3/2, Cu^{+} 2p1/2, Cu^{2+} 2p3/2, and Cu^{2+} 2p1/2 were located at 932.82 eV, 952.60 eV, 935.08 eV, and 954.94 eV, respectively (Fig. 1E). Notably, copper predominantly existed in the Cu^{2+} state (91.71%), which further confirmed the successful synthesis of CuPA. Given the remarkable antioxidant properties of PA [31], we evaluated the ability of the CuPA complex to scavenge ROS (H_2O_2 and $\cdot O_2^-$) and its capacity to neutralize DPPH free radicals. Our results indicated that CuPA can significantly reduce $\cdot O_2^-$ levels within the concentration range of 5 to 100 μg mL^{-1} and effectively eliminate DPPH at concentrations between 1 and 5 μg mL^{-1} (Fig. 1F–I). Moreover, CuPA also exhibited considerable catalase-like enzyme activity by decomposing H_2O_2 at various concentrations (Figures S1B-C, Supporting Information). These findings strongly proved that the CuPA complex possess exceptional antioxidant capacities.

Synthesis and characterization of the Ce NPs

Many studies have demonstrated that Ce NPs have excellent antioxidant, antibacterial, and anti-inflammatory properties; notably, their antioxidant effects play a critical role in alleviating oxidative stress-associated diseases [32]. Spherical Ce NPs, approximately 3 nm in diameter with a crystal lattice spacing of nearly 0.32 nm, were synthesized on the basis of previous studies [33], and element mapping analyses confirmed the presence of Ce within these particles (Fig. 2A, B, Figure S2, Supporting Information). The zeta potential of the Ce NPs was + 14.0 mV, and they presented a maximum UV absorption peak at 288 nm (Figure S3, Supporting Information). Figure 2C shows that the Ce–O bond stretching vibrations appeared at 472 cm^{-1} in Ce NPs spectrum [34]. According to the Ce NPs standard (JCPDS No. 34-0394), these nanoparticles exhibited a cubic fluorite structure, and X-ray diffraction (XRD) revealed distinct diffraction peaks at (111), (200), (220), (311), (400), and (331) (Fig. 2D). Together, these data strongly indicate that we successfully synthesized Ce NPs.

The antioxidant efficacy of Ce NPs is contingent upon the transition between Ce^{3+} (reduced state) and Ce^{4+} (oxidized state). Generally, the surface of Ce NPs predominantly consists of Ce^{4+}. However, as the diameter of the Ce NPs decreases, oxygen vacancies are generated, facilitating the presence of Ce^{3+} [35]. The Ce $3d_{3/2}$ and Ce $3d_{5/2}$ peaks in the XPS spectrum indicated that Ce^{3+} constituted 42.85% of the Ce atoms, whereas Ce^{4+} accounted for 57.15%. This implied that the Ce NPs consisted of a mixture of Ce^{4+} and Ce^{3+} at a ratio of approximately 1.3 (Fig. 2E). We subsequently evaluated the antioxidant functions of the Ce NPs. As shown in Fig. 2F–I**,** the Ce NPs notably reduced the $\cdot O_2^-$ and DPPH levels within the concentration range of 1–100 μg mL^{-1}. These results proved that the Ce NPs possessed substantial antioxidant effects by effectively scavenging ROS such as $\cdot O_2^-$ and DPPH radicals. Furthermore, research has shown that Ce NPs can mimic the activities of superoxide dismutase and catalase [36], thereby establishing them as potent ROS scavengers for treating various diseases associated with oxidative stress and inflammation.

Synthesis and characterization of the hydrogels

The GelMA hydrogel was prepared by grafting MA onto gelatin, followed by curing with LAP and UV irradiation. The ^1H NMR spectrum of GelMA exhibited two distinct peaks at 5.3 and 5.5 ppm, confirming the successful incorporation of MA into the gelatin matrix. In addition, the degree of functionalization (DoF) of MA in the synthesized GelMA was approximately 69% (Figure S4, Supporting Information) [3]. The GCP and GC hydrogels were created by integrating CuPA complexes or Ce NPs into the GelMA framework, followed by curing with LAP and UV exposure. Scanning electron microscopy (SEM) and elemental analysis revealed that the GelMA, GC, and GCP hydrogels possessed a porous network structure, with no significant differences in pore size observed among the groups (Fig. 3A, B). Additionally, the copper in the GCP hydrogel and cerium in the GC hydrogel were uniformly distributed throughout the network (Fig. 3C, D). Figure 3E presents images of GelMA, GC, and GCP hydrogels subjected to UV irradiation, illustrating their transformation from a liquid state to a solid state upon UV exposure.

The prominent peaks observed in the FTIR spectrum of gelatin were broad, appeared within the ranges of 3300 to 2500 cm^{-1} and 3700 to 3200 cm^{-1}, and were attributed to the O–H stretching vibrations associated with the

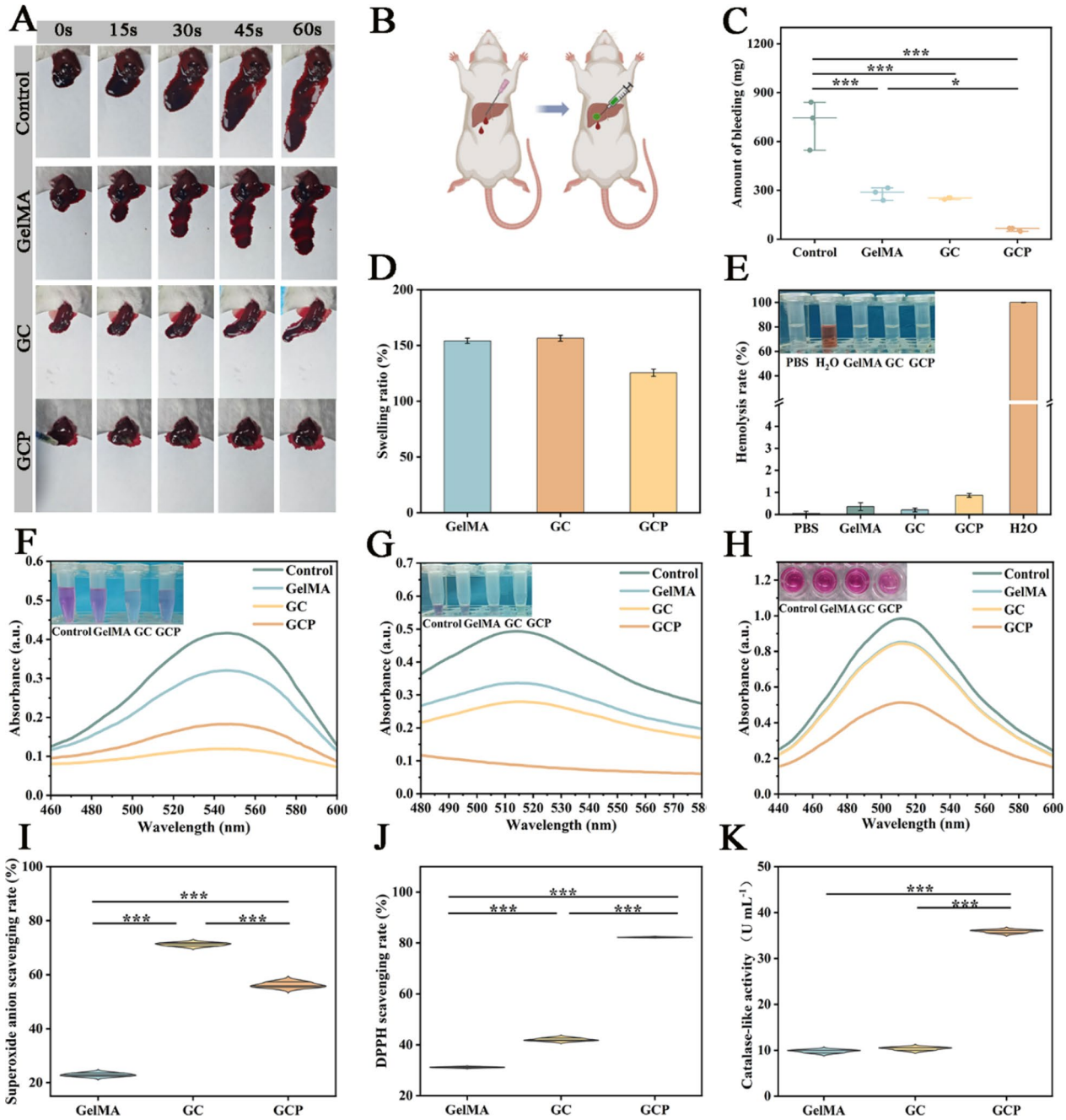

Fig. 4 Characterization, antioxidation capacities, and catalase-like activity of hydrogels. **A** Evaluation of the hemostatic capability of hydrogels. **B** Schematic illustration of the rat liver injury model and hydrogel intervention. **C** Quantification of bleeding volume in rat livers following hydrogel administrations. **D** Swelling ratio of hydrogels. **E** Hemocompatibility assessment of hydrogels. **F**, **I** Superoxide anion scavenging capacity of hydrogels. **G**, **J** DPPH radical scavenging capacity of hydrogels. **H**, **K** Catalase-like activity of different hydrogels. n = 3, mean ± SD, ***p* < 0.05, ****p* < 0.01, *****p* < 0.001

carboxyl and hydroxyl groups, which are characteristic features of gelatin. The peaks at 3423 and 3077 cm^{-1} in the gelatin, GelMA, and GCP spectra were ascribed to N–H bond stretching vibrations. In addition, a peak at 1647 cm^{-1} indicated the stretching vibrations of the C=O bond, whereas the peak at 1540 cm^{-1} represented the C–N bond stretching vibrations and N–H bond bending vibrations. Compared with the spectrum of gelatin, the addition of MA led to a less intense absorption peak in the spectrum of GelMA. This reduction can be attributed

primarily to the acylation reaction that occurred between the carbonyl groups on MA and the hydroxyl groups on gelatin, which notably attenuated the absorption peak related to the O–H stretching vibration. Furthermore, the intensity of this absorption peak in the GCP hydrogel spectrum was lower than that in the GelMA spectrum, likely because the molecular structure of GelMA was altered by the introduction of the CuPA complexes (Fig. 3F).

Before investigating the effects of the GCP hydrogel on diabetic wound healing in rats, we conducted a comprehensive assessment of its fundamental properties, including injectability, self-healing, adhesion, hemostasis, swelling, degradation, permeability, breathability, and hemocompatibility. Figure 3G shows that the GCP hydrogel exhibited excellent shear-thinning behavior; specifically, its viscosity progressively decreased as the shear rate increased. In addition, the GCP hydrogel was placed in a syringe and continuously squeezed to form the letters "NJMU". This suggested that GCP has exceptional injectability, which can be attributed to the integration of CuPA into GelMA, along with the introduction of Schiff base bonds and copper–catechol coordination bonds.

Given that the normal activities of animals may lead to the detachment and fracture of hydrogels, the GCP hydrogels needed to possess adequate self-healing and adhesion properties. Thus, we evaluated the self-healing capabilities of GCP by performing the strain amplitude sweeps and cyclic strain recovery tests using a rheometer. In the strain amplitude sweeps tests, the loss modulus (G") exceeded the storage modulus (G') when the strain reached 294.7% at a constant frequency of 1 Hz, indicating a change from the solid state to the liquid state (Fig. 3H). In the cyclic strain recovery trials, G' surpassed G" under an applied 5% strain, demonstrating that the hydrogel maintained its solid form. However, G" became larger than G' when the strain was increased to 500%, resulting in the gel transforming into a liquid state and a shift from elastic deformation to viscous deformation. The GCP hydrogel demonstrated transitions between the solid and liquid states as the strain varied from 5 to 500%. Notably, the hydrogel can revert to its original state after being subjected to three cycles at 5% strain (Fig. 3I). These observations underscored the remarkable self-healing properties of the GCP hydrogel, as illustrated in Fig. 3J. The entire process primarily involved the fracture and reversible recombination of Schiff base bonds and copper–catechol coordination bonds. Furthermore, we evaluated the adhesion characteristics of the GCP hydrogel via the use of biological tissue from C57BL/6 mice and nonbiological substrates. The results clearly indicated that GCP had outstanding adhesion performance. Specifically, GCP can effectively adhere to the heart, liver, spleen, and kidney of mice (Fig. 3K) and different bottle surfaces, such as plastic and glass (Figure S5, Supporting Information). The adhesion performance of the GCP hydrogel may be associated with interactions between the polyphenol groups within the hydrogel and the amino and hydroxyl groups present in the tissue [3, 37].

Because blood is lost during the construction of full-thickness skin wounds in rat models, we also investigated the hemostatic properties of the hydrogels. We utilized 6-week-old SD rats to establish a liver injury model and assessed the hemostatic effects of different hydrogels within 1 min after application (Fig. 4A, B). The results indicated that the GelMA, GC, and GCP hydrogels exhibited varying degrees of hemostatic efficacy; notably, treatment with the GCP hydrogel significantly reduced bleeding to 60.53 ± 10.60 mg (Fig. 4C). The hemostatic functions of the GelMA and GC hydrogels were attributed primarily to their rapid absorption of platelets from the blood and formation of a gel-like substance, which created a pressure barrier that facilitates blood clotting [38]. In the GCP hydrogel, the catechol groups within the CuPA complexes synergistically interact with the GelMA matrix to facilitate hemostasis by recruiting calcium ions to vascular smooth muscle cells, thereby promoting vascular contraction [3].

When a hydrogel is applied to a diabetic wound, it effectively absorbs interstitial fluid from the affected area, thereby mitigating the risk of recurrent bacterial infections. Additionally, the hydrogel degrades within the wound microenvironment, facilitating the release of copper and PA. Moreover, the RGD sequence in GelMA enhances cellular adhesion and is involved in biological processes such as cell signaling, proliferation, and differentiation. The MMP sequence in GelMA is selectively recognized and enzymatically degraded by matrix metalloproteinases present at the wound site, promoting material degradation while supporting tissue reconstruction. Therefore, it is essential to assess the swelling and degradation properties of hydrogels. Our results revealed that the swelling rates of the GelMA, GC, and GCP hydrogels were 154.27%, 156.60%, and 125.55%, respectively (Fig. 4D). Notably, the swelling rate of the hydrogel decreased from 154.27% to 125.55% following the incorporation of the CuPA complexes; this finding indicates that CuPA enhanced network crosslinking to some extent. Furthermore, the GelMA and GC hydrogels fully degraded in approximately 60 h, whereas the GCP hydrogel degraded entirely in approximately 72 h because of its greater abundance of Cu–catechol coordination bonds and Schiff base bonds. Type I/II collagenase significantly accelerates the degradation of GelMA, GC, and GCP hydrogels, primarily due to the enzymatic cleavage of gelatin. Both GelMA and GC hydrogels

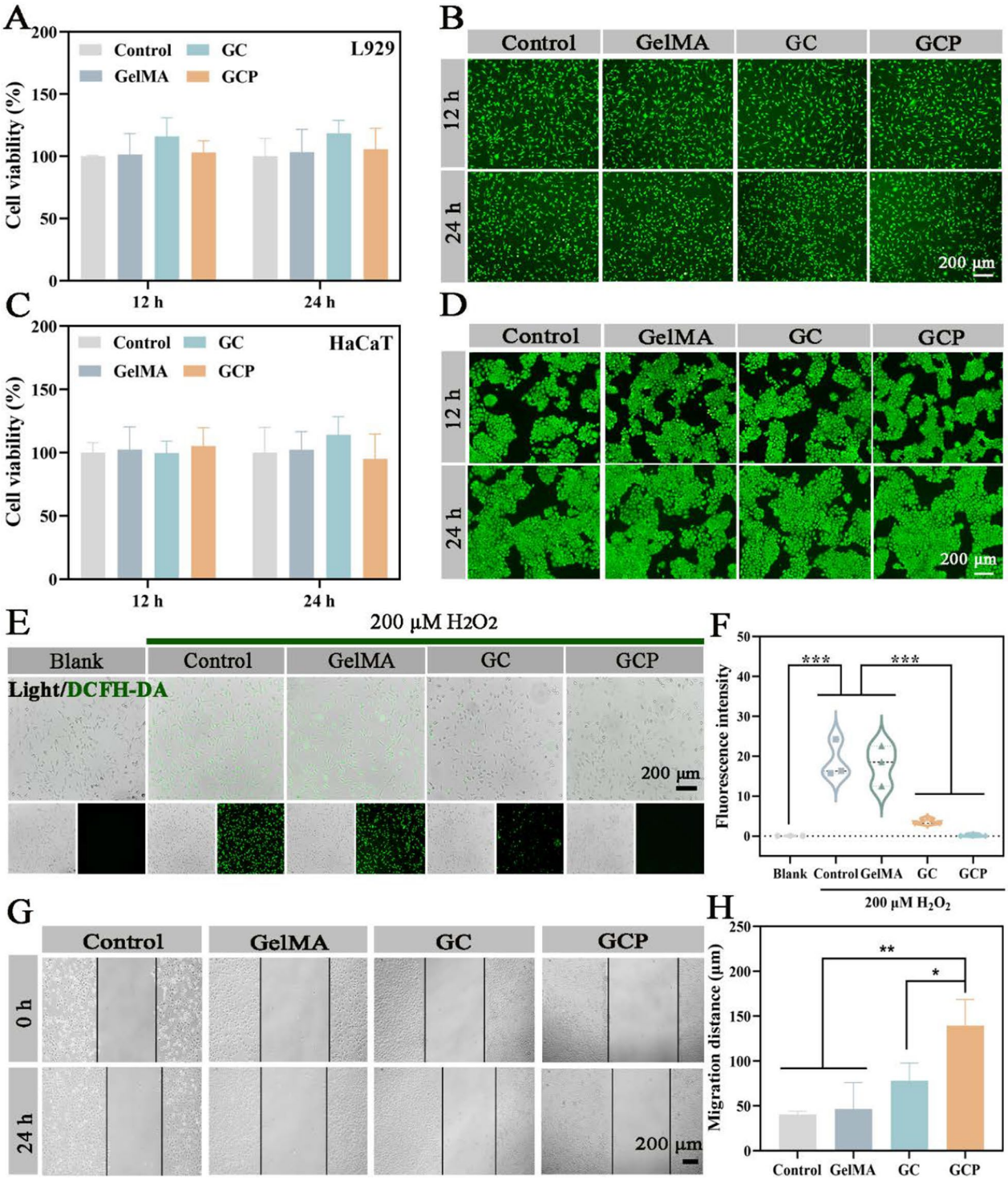

Fig. 5 Cytocompatibility, intracellular ROS scavenging, and cell migration promotion of hydrogels. **A** Cell viability and **B** Calcein-AM/PI staining of L929 cells cultured with hydrogels for 12 and 24 h (scale bar: 200 μm). **C** Cell viability and **D** Calcein-AM/PI staining of HaCaT cells treated with hydrogels for 12 and 24 h (scale bar: 200 μm). **E** Intracellular ROS levels in L929 cells treated with various hydrogels (scale bar: 200 μm). **F** Mean fluorescence intensity of ROS among the groups. **G** Migration of L929 cells treated with hydrogels for 24 h (scale bar: 200 μm). **H** Quantification of migration distance in L929 cells treated with hydrogels. n = 3, mean ± SD, ***p* < 0.05, ****p* < 0.01, *****p* < 0.001

exhibited approximately 80% degradation within 4 h, while the degradation rate of GCP hydrogel was slightly slower compared to GelMA and GC (Figure S6, Supporting Information). Due to the difficulty of water molecules penetrating highly crosslinked networks, the water retention capacity of hydrogels typically decreases. Our results also revealed that the triple-network crosslinked GCP exhibits slightly weaker water retention compared to GelMA and GC (Figure S8B, Supporting Information).

The exceptional permeability and breathability of the hydrogels facilitate the maintenance of a moist wound environment, enhance gas exchange, and promote accelerated wound healing. We measured their dynamic water contact angles (WCAs) at 0 min and 5 min to indirectly evaluate the permeability of hydrogels. The WCAs of GelMA were 44.1° and 23.4° at 0 min and 5 min, respectively; for GC, they were 107.8° and 99.3°; and for GCP, they were 63.2° and 44.5° (Figure S7, Supporting Information). These results indicate that GelMA and GCP exhibit excellent hydrophilicity, while GC demonstrates a certain degree of hydrophobicity. Over the 5-min period, the water contact angles of GelMA, GC, and GCP changed by 20.7°, 8.5°, and 18.7°, respectively, indicating that the permeability of the hydrogels follows the order: GelMA > GCP > GC. The minimal change in GC is likely due to its lower affinity for water, while the smaller change in GCP compared to GelMA may be attributed to its enhanced network crosslinking, which limits water penetration. In addition, the water vapor transmission rates (WVTR) of GelMA, GC, and GCP were determined to be 1989, 2064, and 1808 mg m^{-2} d^{-1}, respectively (Figure S8A, Supporting Information). These values exceed those of most previously reported hydrogels [39], indicating their superior capacity to maintain an optimal moist wound environment and accelerate diabetic wound healing. Furthermore, the results provide additional evidence that the incorporation of PA enhances the mechanical properties of the GCP hydrogel.

Additionally, the hydrogels should also demonstrate superior hemocompatibility, meaning that no significant hemolysis should occur upon material introduction. As shown in Fig. 4E, no apparent hemolysis was observed in any of the hydrogel treatment groups. The hemolysis rates were as follows: GelMA at 0.36% ± 0.18%, GC at 0.20% ± 0.09%, and GCP at 0.87% ± 0.09%. All these values remained below the established acceptable hemolysis rate threshold of 5% [38]. GelMA is considered a material with outstanding biocompatibility, and the catechol groups in the GCP hydrogels can maintain cell membrane integrity and mitigate hemolysis by alleviating oxidative stress and inflammation within cells [40]. On the basis of the abovementioned results, the GCP dressings has been proven to have outstanding fundamental properties, such as self-healing, adhesion, hemostasis, swelling, degradation, permeability, breathability, and hemocompatibility, which are required for the treatment of infected diabetic wounds.

Antioxidant capacities and enzyme-like activities of the hydrogels

In individuals with diabetes, persistently elevated blood glucose levels stimulate cellular mitochondria to produce large amounts of ROS. The overproduction of ROS can exacerbate inflammation and facilitate the onset of chronic inflammatory conditions such as arthritis and atherosclerosis [41]. In addition, high ROS levels may damage vascular endothelial cells, resulting in compromised blood vessel function, reduced wound healing rates, and increased susceptibility to cardiovascular diseases [42]. To address the challenge of increased reactive ROS levels in diabetic wounds, we investigated the antioxidant properties of the composite hydrogels via the use of antioxidation kits and mouse fibroblasts (L929 cells). The findings indicated that the GCP and GC hydrogels demonstrated pronounced abilities to scavenge $\cdot O_2^-$ and DPPH free radicals, and the GCP hydrogel exhibited notable catalase-like activity (Fig. 4F-K). Moreover, L929 cells were treated with 200 μM H_2O_2 and different hydrogels, and the GCP and GC hydrogels both displayed exceptional efficacy in terms of intracellular ROS clearance (Fig. 5E, F). Overall, the GCP hydrogel exhibited a robust capacity for eliminating ROS. This efficacy may be attributed to the increased antioxidant potential of CuPA when functional groups such as aldehydes and hydroxyls from polyphenolic bioactive compounds are integrated [43, 44]. These functional groups can directly transfer their active hydrogen atoms to $\cdot O_2^-$, DPPH, and H_2O_2, thereby neutralizing ROS activity [45].

A material with outstanding biocompatibility is generally thought to not induce significant toxicity, which is

(See figure on next page.)

Fig. 6 Anti-inflammatory and pro-angiogenic functions of hydrogels. **A** Schematic representation of the anti-inflammatory properties of hydrogels. **B–D** Relative mRNA expression levels of iNOS, IL-1β, and IL-6. **E** Western blot images showing iNOS, IL-1β, and IL-6 protein expression across groups. **F–H** Relative protein expression levels of iNOS, IL-1β, and IL-6. **I** Representative images of tube formation by HUVECs in the presence of different hydrogels. **J** Number of junctions and **K** meshes formed by HUVECs among groups. **L** Relative mRNA expression and **M** protein concentration of VEGF in HUVECs treated with hydrogels. n = 3, mean ± SD, ***p** < 0.05, ****p** < 0.01, *****p** < 0.001

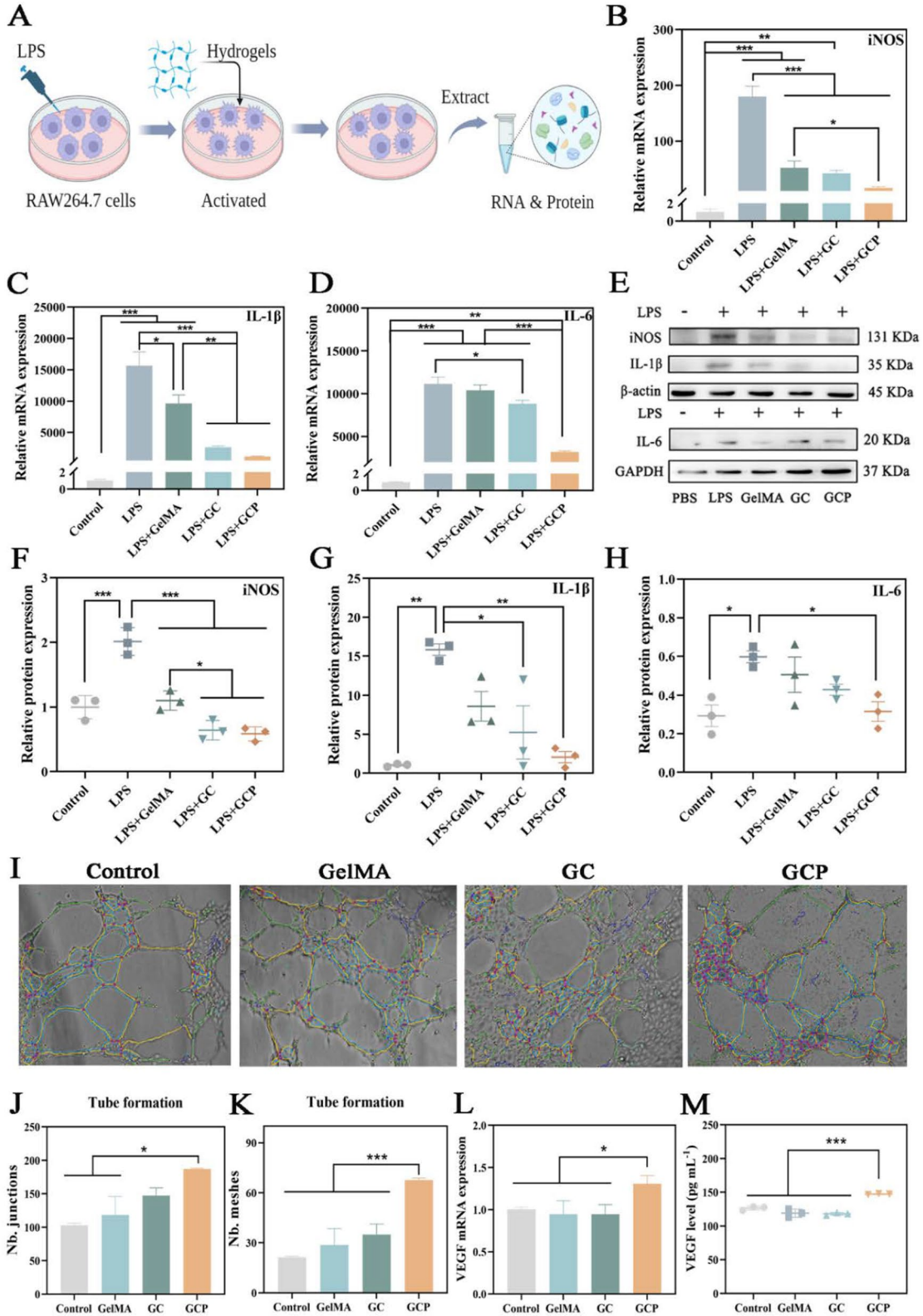

Fig. 6 (See legend on previous page.)

crucial for preserving the health of human cells and tissues. Therefore, we assessed the biocompatibility of the synthesized hydrogels with L929 and human immortalized keratinocytes (HaCaT cells). CCK8 assays and Calcein-AM/PI staining revealed that the viability of L929 and HaCaT cells exceeded 95% after treatment with various hydrogels for 12 and 24 h, with no evident signs of cell death observed (Fig. 5A–D). These results demonstrated that the GelMA, GC, and GCP hydrogels favorable cytocompatibility.

Cell migration promoting, anti-inflammatory and angiogenic capacities of hydrogels

We further investigated the abilities of the hydrogels to promote the migration of L929 and HaCaT cells. Enhanced cell migration facilitates signal communication among wound cells and accelerates wound reconstruction in diabetic rats. After co-culturing the hydrogels with L929 and HaCaT cells, we observed that the GCP hydrogel significantly accelerated cell migration within 24 h compared with cell migration in the control, GelMA, and GC groups (Fig. 5G, H, and Figure S9 in Supporting Information). This finding indicated that the GCP hydrogel exhibited a robust capacity to promote fibroblasts and epidermal cells migration and demonstrated great potential as a dressing to accelerate wound healing.

Elevated blood glucose levels trigger an enhanced inflammatory response in individuals with diabetes, promoting the body to produce various inflammatory factors such as iNOS, IL-1β, and TNF-α. Sustained release of these mediators may result in chronic inflammation and immune dysfunction [46]. Infected diabetic wounds also exhibit considerable inflammation. Thus, we evaluated the anti-inflammatory performance of the synthesized materials by coculturing hydrogels, 1 μg mL^{-1} LPS, and mouse monocyte macrophages (RAW264.7 cells). The quantitative real-time PCR (qRT-PCR) and western blot data indicated that the GC and GCP hydrogels significantly reduced the mRNA and protein expression levels of iNOS, IL-1β, and IL-6 in RAW264.7 cells (Fig. 6A–H). Furthermore, the GC and GCP hydrogels displayed exceptional efficacy in decreasing the fluorescence intensity of CD86 (Figures S10A-B, Supporting Information). Notably, the GCP hydrogels demonstrated the most pronounced anti-inflammatory effects, likely attributable to the beneficial anti-inflammatory properties of polyphenolic compounds. Studies have demonstrated that curcumin exerts anti-inflammatory effects by modulating signaling pathways such as the TLR4/NF-κB and JAK/STAT pathways [47, 48]. Quercetin and its derivatives inhibit inflammatory responses by suppressing the expression of inflammatory mediators, including TNF-α and IL-6, and regulating the PI3K/AKT signaling pathway [49]. Furthermore, polyphenolic compounds can alleviate systemic inflammation by modulating the gut microbiota and its metabolites, such as short-chain fatty acids (SCFAs) [50]. Our research further revealed that the anti-inflammatory properties of the GCP hydrogel containing PA may be associated with the inhibition of NF-κB activation. Specifically, the GCP hydrogel was observed to markedly downregulate the mRNA expression level of NF-κB and decrease the protein expression ratio of phospho-NF-κB p65 to total NF-κB p65 (Figures S10C-E, Supporting Information).

In addition to elevated levels of inflammation and oxidative stress, the management of diabetic wounds is further complicated by challenges in terms of angiogenesis. Prolonged hyperglycemia leads to human umbilical vein endothelial cells (HUVECs) and vascular dysfunction [51]. These difficulties in angiogenesis and vascular repair hinder the reconstruction of diabetic wounds. Adequate regenerated vasculature is essential for delivering efficient immune cells, nutrients, and oxygen to the wound site, thereby promoting tissue remodeling [52]. Therefore, multifunctional hydrogel dressings should possess properties that facilitate angiogenesis. We evaluated the angiogenic effects of the hydrogels by coculturing them with HUVECs; then, images of tube formation were acquired, and RNA and protein from HUVECs were extracted and measured via qRT-PCR and an ELISA kit. For the protein assays, we established a standard curve for VEGF ranging from 0 to 200 pg mL^{-1} (Figure S11, Supporting Information). As shown in Figs. 6I–K, the GCP hydrogel increased the number of junctions and meshes during vessel formation. In addition, the VEGF mRNA and protein contents and ANG mRNA level increased following GCP intervention (Figs. 6L, M, Figure S12, Supporting Information), which suggested that GCP can greatly

(See figure on next page.)

Fig. 7 Antibacterial properties of hydrogels and transcriptomic analysis of *S. aureus* treated with CuPA. **A** Dilution plate images of *S. aureus* and *E. coli* treated with hydrogels. **B** SEM images of *S. aureus* and *E. coli* under various hydrogel conditions (scale bar: 1 μm). **C** SYTO9/PI staining of *S. aureus* and **D** *E. coli* treated with hydrogels (scale bar: 1 mm). **E** Viability of *S. aureus* and **F** *E. coli* following hydrogel treatment. **G** Venn diagram illustrating the gene features of *S. aureus*. **H** Volcano plot indicating upregulated (n = 277) and downregulated (n = 112) genes in *S. aureus* treated with CuPA ($|\log_2 FC| \geq 2$, $p < 0.05$). **I** KEGG enrichment analysis of downregulated DEGs in *S. aureus* treated with CuPA. **J** Expression of downregulated genes in aminoacyl-tRNA biosynthesis and ABC transporter pathways in *S. aureus* treated with CuPA. n = 3, mean ± SD, ***p** < 0.05, ****p** < 0.01, *****p** < 0.001

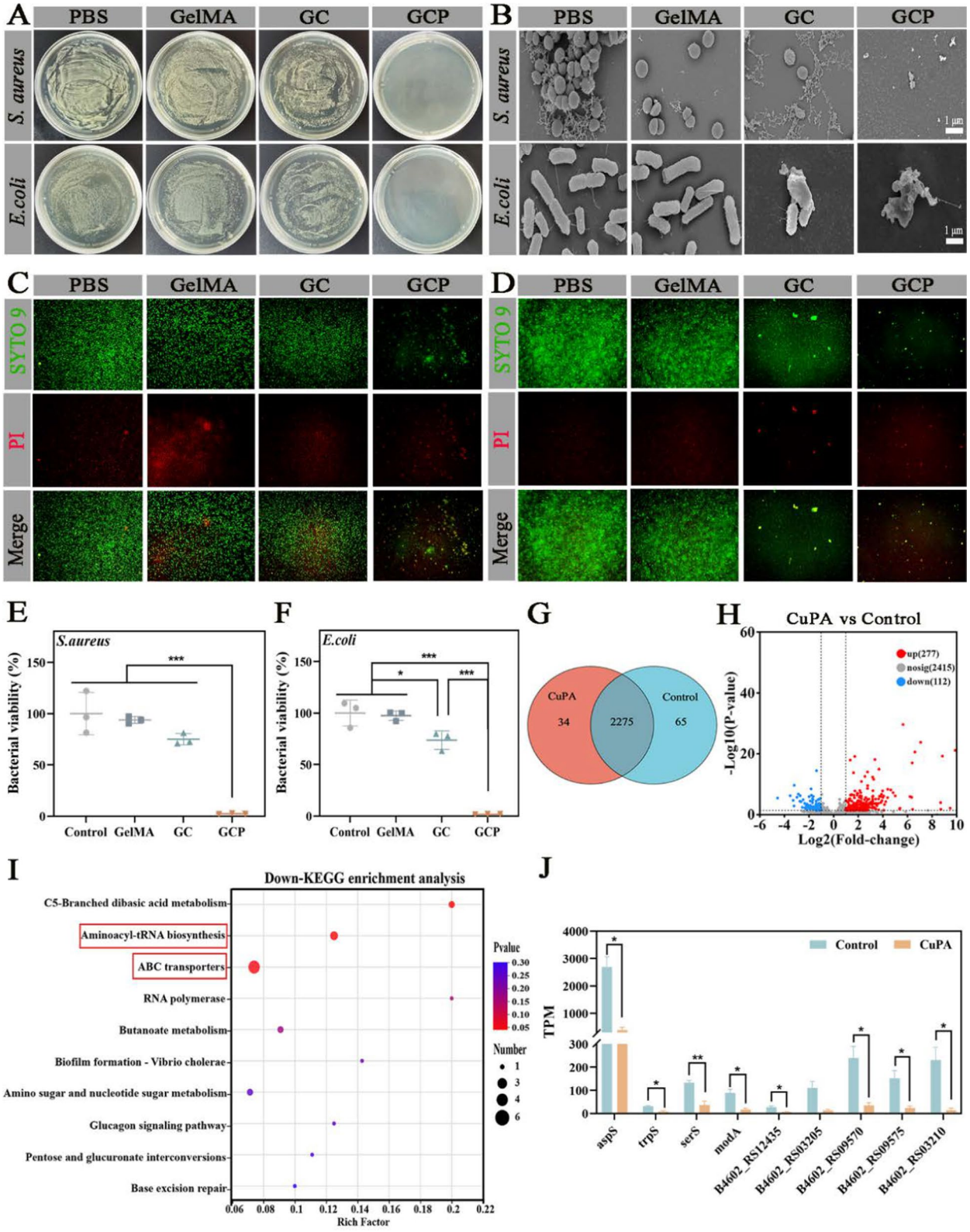

Fig. 7 (See legend on previous page.)

increase angiogenesis, potentially due to the copper-mediated activation of the angiogenic pathway [53].

Antibacterial properties of various hydrogels

One of the primary challenges associated with wound healing in diabetic patients is infections caused by bacteria such as *S. aureus*, *E. coli*, *K. pneumoniae*, and *Pseudomonas aeruginosa*, with *S. aureus* considered the most prominent pathogenic organism [54]. These bacterial infections can trigger an inflammatory response that may result in fluctuations in blood glucose levels in individuals with diabetes. In addition, bacterial infection can lead to more severe complications, such as cellulitis and bacteremia [55, 56]. Thus, antibacterial functions are vital for hydrogels to combat potential bacterial infections in diabetic wounds. The antibacterial efficacy of GCP was assessed through dilution plating, SEM, and SYTO9/PI staining assays. Figure 7A, E, and F show that GCP significantly reduced the activities of *S. aureus* and *E. coli*, and SEM analysis revealed notable alterations in the inherent morphology of both bacterial species (Figure S13, Supporting Information). The original spherical and rod-shaped structures of the bacteria were compromised, leading to diminished viability and eventually, death (Fig. 7B). These findings suggested that the GCP hydrogel had robust antibacterial efficacy against *S. aureus* and *E. coli*, and SYTO9/PI staining confirmed this conclusion. SYTO9 labels the nuclei of bacteria and emits green fluorescence, whereas PI penetrates compromised membranes of dead bacteria to stain their nuclei and emits red fluorescence. Thus, SYTO9 labels both viable and nonviable bacteria, whereas PI specifically labels dead bacteria only. The results indicated that the viable counts of *S. aureus* (Fig. 7C) and *E. coli* (Fig. 7D) markedly decreased following GCP hydrogel treatment.

After evaluating the specific antibacterial properties of the GCP hydrogels, we further explored the potential bactericidal mechanism of the CuPA complex, the critical component of the GCP hydrogel responsible for its antibacterial function. *S. aureus* was cultured in two groups (Control and CuPA), with three replicate samples in each group, and RNA was extracted post-coculture for transcriptomic sequencing. The constructed Venn diagram revealed that 65 genes were expressed in untreated *S. aureus* only, whereas 34 genes were expressed in CuPA-treated *S. aureus* only, and 2275 genes were identified in both groups (Fig. 7G). Analysis of this dataset showed that among the differentially expressed genes (DEGs) after CuPA treatment, 277 genes were upregulated and 112 genes were downregulated (Fig. 7H; Figure S14, Supporting Information). The DEGs from both the Control and CuPA groups are also presented in a heatmap (Figure S15, Supporting Information). KEGG enrichment analysis of revealed that certain pathways, including aminoacyl-tRNA biosynthesis and ABC transporters, were significantly enriched in the downregulated DEGs (Fig. 7I). The expression of aspS, trpS, and serS in the aminoacyl-tRNA biosynthesis pathway and modA, B4602_RS12435, B4602_RS03205, B4602_RS09570, B4602_RS09575, and B4602_RS03210 in the ABC transporter pathway of *S. aureus* decreased following CuPA treatment (Fig. 7J). Aminoacyl-tRNA facilitates the transfer of amino acids to ribosomes, promoting bacterial protein synthesis [57]. The ABC transporter is essential for nutrient uptake by and toxin secretion from bacteria and may also contribute to antibiotic resistance [58]. Therefore, the GCP hydrogel may impede the growth and reproduction of *S. aureus* by downregulating certain genes associated with ABC transporters and bacterial protein synthesis. Furthermore, our results also demonstrated that CuPA treatment altered certain cellular components, biological processes, and molecular functions (Figure S16, Supporting Information). GO enrichment analysis of the upregulated DEGs revealed increased in oxidoreductase activity and a heightened stress response to copper ions, which may also contribute to *S. aureus* mortality (Figure S17, Supporting Information). Enhanced oxidoreductase activity can eradicate bacteria by facilitating ROS generation and interfering with microbial metabolism [59].

The GCP hydrogel enhances wound healing in infected diabetic rats

Given that the GCP hydrogel exhibited suitable fundamental properties and exceptional antioxidant, anti-inflammatory, antibacterial, and angiogenic effects, we further investigated the ability of GCP to promote wound healing in 6-week-old SD rats. Figure 8A illustrates the

(See figure on next page.)

Fig. 8 GCP hydrogel accelerates wound healing in infected diabetic rats. **A** Schematic diagram of the experimental design for the in vivo wound healing study. **B** Images of wounds sites in rats across experimental groups on days 0, 2, 4, 7, 10, and 14. **C** Temporal wound healing trajectories depicted by color-coded wound areas: blue (day 0), yellow (day 2), green (day 4), orange (day 7), pink (day 10), and red (day 14). **D** Quantitative analysis of wound area reduction over time in each group. **E** Representative H&E staining and **F** Masson's trichrome staining images of wound tissues on days 7 and 14 (scale bar: 500 μm and 200 μm, respectively). D: Dermis, Ep: Epidermis, H.F: Hair follicle, Sc. G: Sebaceous gland. **G** Epidermal thickness and **H** collagen density in wound tissues among the groups. n = 3, mean ± SD, ***p** < 0.05, ****p** < 0.01, *****p** < 0.001

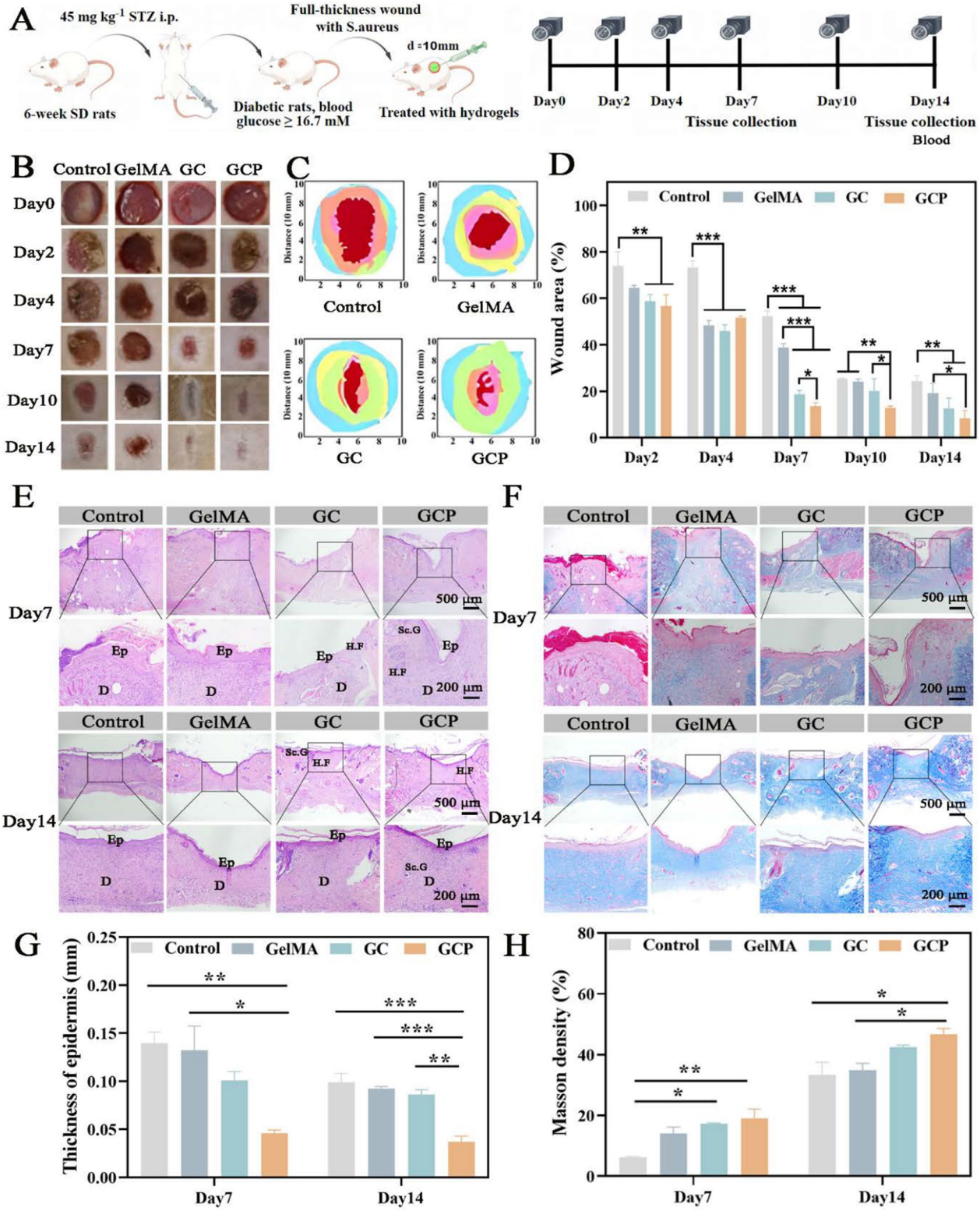

Fig. 8 (See legend on previous page.)

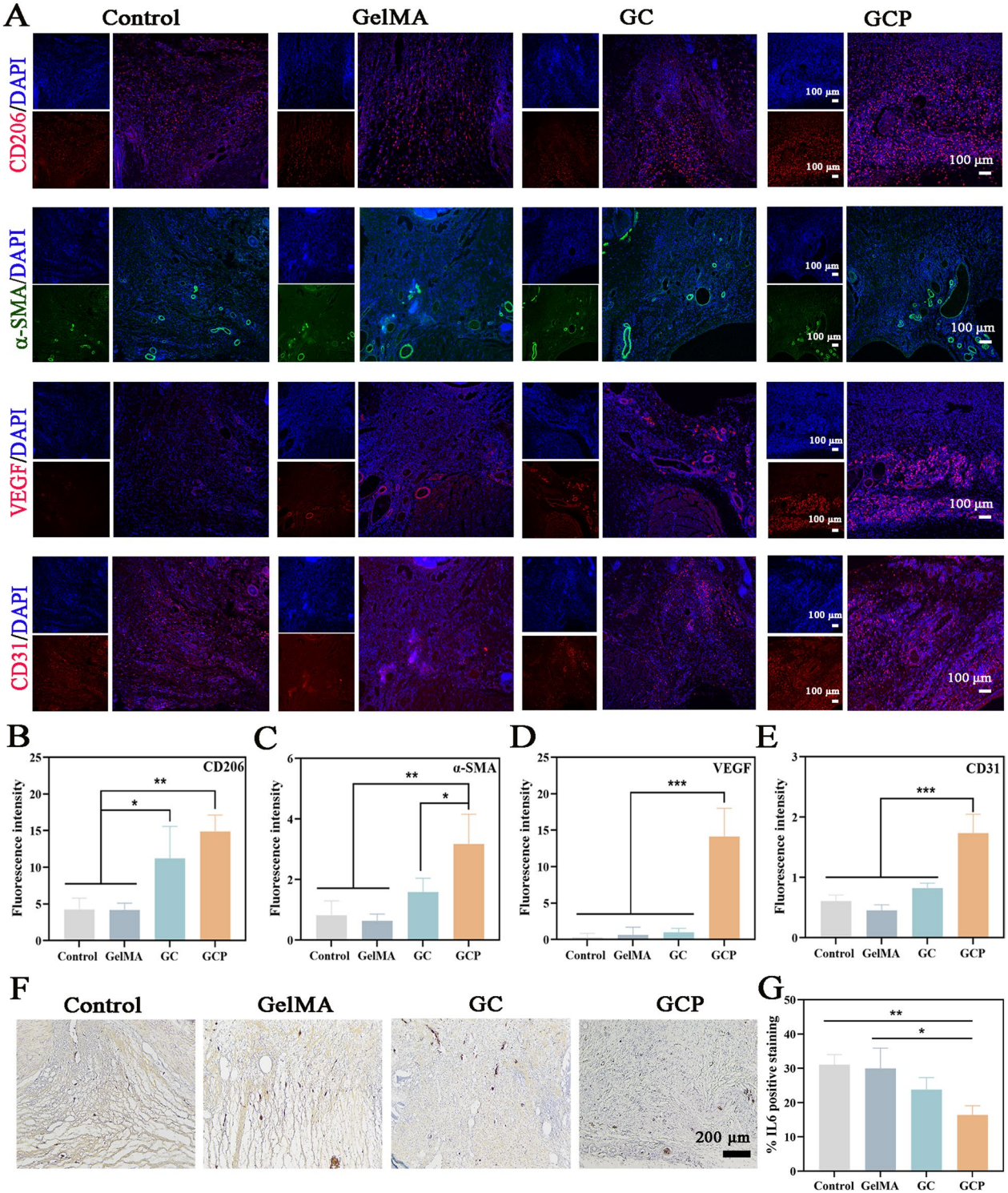

Fig. 9 Anti-inflammation and pro-angiogenic effects of GCP hydrogel in infected diabetic wounds. **A** Representative immunofluorescence staining images of CD206, α-SMA, VEGF, and CD31 in wound tissues across groups (scale bar: 100 μm). **B–E** Quantitative analysis of fluorescence intensity for CD206, α-SMA, VEGF, and CD31 in wound tissues. **F** Immunohistochemical staining images of IL6 in wound tissues (scale bar: 200 μm). **G** Percentage of IL6-positive staining area in wound tissues among the groups. n = 3, mean ± SD, ***p* < 0.05, ****p* < 0.01, *****p* < 0.001

animal experimental design. We established a diabetic rat model through the intraperitoneal injection of 45 mg kg^{-1} streptozotocin. On Days 3 and 7, the blood glucose levels of the rats were randomly examined, and those with values equal to or greater than 16.7 mM were considered diabetic. The diabetic rats were then randomly allocated to four groups: the Control, GelMA, GC, and GCP groups. After anesthesia, a 10 mm full-thickness circular wound was created on the backs of each rat. In addition, 10 μL of *S. aureus* (1.0×10^8 CFU mL^{-1}) and 100 μL of different solidified hydrogels were applied to the wounds. The day of surgery was designated Day 0. Images of the infected wounds from each group of diabetic rats were acquired on Days 0, 2, 4, 7, 10, and 14. On Days 7 and 14, wounds from each group were harvested for hematoxylin–eosin (H&E) staining and Masson's trichrome staining to quantify the epidermis thickness and collagen density. On Day 14, blood and other vital tissues from the rats were also collected to assess the biocompatibility of the hydrogels. Furthermore, immunofluorescence (IF) and immunohistochemical (IHC) staining were performed on wound sections obtained on Day 7 to assess the angiogenic and anti-inflammatory capacities of the hydrogels during wound healing.

Images of the infected wounds from each group of diabetic rats are shown in Fig. 8B, and the wound healing trajectory is depicted in Fig. 8C. The results revealed a progressive reduction in the wound area over time in all of the groups, with the GCP hydrogel exhibiting the most pronounced wound healing promotion. Specifically, from Day 2 until the conclusion of the trial, the wound areas of the rats treated with GC or GCP were markedly smaller than those of the control rats. In addition, a notable reduction in the wound area in the GCP group compared with the GC group was noted on Days 7 and 10 (Fig. 8D). H&E staining revealed that the hydrogel-treated groups exhibited a reduction in neovascularization and inflammatory cell infiltration compared to the control group. (Figure S18, Supporting Information) [60, 61]. Furthermore, the formation of hair follicles and sebaceous glands was observed in both the GC and GCP groups on Days 7 and 14 [62, 63]. In addition, GCP hydrogel intervention significantly reduced the epithelial gap and increased the collagen density in the wounds of diabetic rats (Fig. 8E–H). These findings suggest that the GCP hydrogel can effectively facilitate infected diabetic wound healing by accelerating re-epithelialization, stimulating collagen fiber formation, and promoting the regeneration of skin appendages [64].

The challenges related to inflammation and angiogenesis are the primary factors that impede wound healing in diabetic patients. Our experimental results demonstrated that the GCP hydrogel exhibited anti-inflammatory and proangiogenic effects in vitro. Therefore, we aimed to further investigate whether the GCP hydrogel has significant anti-inflammatory and proangiogenic functions in infected wounds in diabetic rat models through IF and IHC staining for CD206, IL6, α-SMA, VEGF, and CD31 on Day 7 (Fig. 9). CD206 and IL6 are well-established markers of inflammatory activity, whereas increased angiogenesis is indicated by elevated VEGF expression. CD31 is widely recognized as a marker for vascular endothelial cells, whereas α-SMA serves as an indicator for smooth muscle cells [65]. Elevated expression levels of CD31 and α-SMA create a conducive foundational environment for angiogenesis. The results indicated that GCP significantly increased the mean fluorescence intensity of CD206, α-SMA, VEGF, and CD31 and reduced the IL6-positive area in diabetic rats. These data suggest that GCP possesses notable anti-inflammatory and angiogenic properties in infected diabetic wounds.

Biocompatibility of the GCP hydrogel

Finally, we assessed the in vivo biocompatibility of the hydrogels by measuring routine blood and biochemical indices and observing pathological alterations in the heart, liver, spleen, lung, and kidney across different groups on Day 14. Our findings revealed that no evidence of organ damage or pathological changes in the groups treated with hydrogels (Figure S19, Supporting Information). In addition, no significant variations in routine blood and biochemical markers were observed among the groups (Figure S20, Supporting Information). These results demonstrated that the GCP hydrogel exhibited excellent biocompatibility.

Advantages of the GCP hydrogel

In comparison to existing hydrogels utilized for diabetic wound management, such as silver-based dressings and growth factor-incorporated hydrogels, the copper-integrated GCP hydrogel synthesized in our study demonstrates superior attributes in antimicrobial efficacy, biosafety, pro-angiogenic capacity, and cost-effectiveness. Regarding antimicrobial performance and biosafety, silver exhibits broad-spectrum antibacterial activity, effectively suppressing the proliferation of common bacterial strains (e.g., achieving over 99% inhibition rates against *E. coli* and *S. aureus*) and drug-resistant pathogens [66]. However, the high chemical activity, strong cellular penetration capacity, and significant bioaccumulation potential of silver ions and nanoparticles may lead to localized toxicity upon their release from hydrogels [67]. As for copper, it also demonstrates broad-spectrum antibacterial activity, with the GCP hydrogel in this study achieving inhibition rates of approximately 98% against *S. aureus* and *E. coli*. As an essential trace element in the

human physiology, copper possesses a tightly regulated metabolic mechanism and a lower toxicity risk, rendering it significantly superior to silver-based dressings in terms of biosafety [21]. Furthermore, while hydrogels containing growth factors exhibit favorable biocompatibility, their inherent instability and lack of antimicrobial functionality may limit their long-term efficacy in the management of diabetic wounds.

In terms of pro-angiogenic capacity, silver itself lacks intrinsic angiogenic properties. Although VEGF can effectively stimulate wound angiogenesis, it is susceptible to degradation by certain proteases in the wound microenvironment [68]. In contrast, copper-based hydrogels have been demonstrated to exhibit robust stability and potential angiogenic effects [69]. In this study, we observed that the GCP hydrogel increased the number of junctions and meshes during vessel formation and upregulated the fluorescence expression of VEGFA, CD31, and α-SMA in the wounds of diabetic rats, potentially mediated through the copper-induced activation of HIF-1α/VEGF signaling pathway [70]. Additionally, hydrogels containing silver or growth factors are expensive, whereas copper-based materials have a lower cost, and copper exhibits catalytic activity comparable to platinum. Furthermore, the potent antibacterial properties of copper-based hydrogels can reduce the reliance on antibiotics, thereby mitigating the risk of bacterial resistance. Collectively, these advantages underscore the potential of copper-based GCP hydrogels for future clinical applications in the diabetic wound management. In future research, the hydrogels can be further optimized by incorporating additional functional components, such as other metals (e.g., zinc, magnesium), bio-functional polysaccharides, or alternative carriers, to enhance its efficacy not only for diabetic wounds but also for other complicated diseases. However, it is important to acknowledge that the clinical efficacy of the GCP hydrogel may be affected by long-term safety and individual variability, which warrant further investigation.

Conclusions

Herein, a dual cross-linked multifunctional injectable hydrogel consisting of GelMA and CuPA complexes was developed through UV light-initiated polymerization of propenyl groups in GelMA and the formation of Schiff base bonds between the amino groups in GelMA and the aldehyde groups in CuPA. Owing to the introduction of CuPA, the as-fabricated GCP hydrogel exhibited an exceptional ability to remodel the wound microenvironment due to its antioxidant, antibacterial, angiogenic, cell migration-promoting, and anti-inflammatory effects. Moreover, the GCP hydrogel exhibited excellent injectability, self-healing, adhesive, hemostatic properties, and biocompatibility. The 16S rRNA sequencing results of *S. aureus* treated with CuPA revealed that the CuPA complexes inhibited the growth and reproduction of *S. aureus* by downregulating certain genes associated with ABC transporters, hindering bacterial protein synthesis, and enhancing oxidoreductase activity, yielding bactericidal effects. This research may provide additional ideas for the development of high-performance wound healing dressings and novel strategies for the treatment of complicated diseases.

Materials and methods

Detailed experimental methods and partial results were submitted in the Supporting Information.

Supplementary Information

The online version contains supplementary material available at https://doi.org/10.1186/s12951-025-03285-2.

Additional file 1.

Acknowledgements
We would like to express our gratitude to BioRender for the expert drawing services.

Author contributions
Z. Z.: Writing original draft, Investigation, Methodology. Y. D.: Investigation, Methodology. H. Y.: Formal analysis, Validation. C. R.: Data curation, Software. P. F.: Investigation, Data curation. Y. J.: Formal analysis, Validation. Y. X.: Supervision, Funding acquisition, Writing, review & editing. J. D.: Supervision, Funding acquisition, Writing, review & editing. L. L.: Supervision, Funding acquisition, Writing, review & editing.

Funding
This research was supported by the National Key Research and Development Program of China (2021YFA1101100) and the National Natural Science Foundation of China (No. 22305217, 82173571).

Data availability
Data will be made available on request.

Declarations

Ethics approval and consent to participate
All animal procedures were approved by the Institutional Animal Care and Use Committee of Nanjing Medical University (Approval No. IACUC-2401017) and were conducted following China's Animal Care and Use Guidelines.

Consent for publication
All authors agree with the publication.

Competing interests
The authors declare no competing interests.

Author details
[1]Center for Global Health, School of Public Health, Nanjing Medical University, 101 Longmian Avenue, Nanjing 211166, China. [2]Sir Run Run Shaw Hospital, School of Medicine, Zhejiang University, 3 East Qingchun Road, Hangzhou 310016, China.

Received: 25 December 2024 Accepted: 2 March 2025
Published online: 18 March 2025

References

1. Collaborators GD. Global, regional, and national burden of diabetes from 1990 to 2021, with projections of prevalence to 2050: a systematic analysis for the Global Burden of Disease Study 2021. Lancet. 2023;402:203–34.
2. Korac B, Kalezic A, Pekovic-Vaughan V, Korac A, Jankovic A. Redox changes in obesity, metabolic syndrome, and diabetes. Redox Biol. 2021;42: 101887.
3. Xie D, Hu C, Jiang C, Xia J, Ye L, Jin Y, Jiang S, Ji Y, Zhang Z, Song H, et al. Incorporating copper-based nanosheets into an injectable self-healing hydrogel enables superb repair of infected diabetic wound. Chem Eng J. 2023;476: 146788.
4. Ma T, Zhai X, Jin M, Huang Y, Zhang M, Pan H, Zhao X, Du Y. Multifunctional wound dressing for highly efficient treatment of chronic diabetic wounds. VIEW. 2022;3:20220045.
5. Peña OA, Martin P. Cellular and molecular mechanisms of skin wound healing. Nat Rev Mol Cell Biol. 2024;25:599–616.
6. Chang M, Nguyen TT. Strategy for treatment of infected diabetic foot ulcers. Acc Chem Res. 2021;54:1080–93.
7. Kharaziha M, Baidya A, Annabi N. Rational design of immunomodulatory hydrogels for chronic wound healing. Adv Mater. 2021;33: e2100176.
8. Moore EE, Moore HB, Kornblith LZ, Neal MD, Hoffman M, Mutch NJ, Schöchl H, Hunt BJ, Sauaia A. Trauma-induced coagulopathy. Nat Rev Dis Primers. 2021;7:30.
9. Wasko R, Bridges K, Pannone R, Sidhu I, Xing Y, Naik S, Miller-Jensen K, Horsley V. Langerhans cells are essential components of the angiogenic niche during murine skin repair. Dev Cell. 2022;57:2699-2713.e2695.
10. Sawaya AP, Stone RC, Brooks SR, Pastar I, Jozic I, Hasneen K, O'Neill K, Mehdizadeh S, Head CR, Strbo N, et al. Deregulated immune cell recruitment orchestrated by FOXM1 impairs human diabetic wound healing. Nat Commun. 2020;11:4678.
11. Zhao M, Kang M, Wang J, Yang R, Zhong X, Xie Q, Zhou S, Zhang Z, Zheng J, Zhang Y, et al. Stem cell-derived nanovesicles embedded in dual-layered hydrogel for programmed ROS regulation and comprehensive tissue regeneration in burn wound healing. Adv Mater. 2024;36: e2401369.
12. Wu J, Wang W, Shen J, Zhou N, Li Y, Tang BZ, Zhang M. A thermosensitive hydrogel with efficient NIR photothermal conversion as injectable wound dressing for accelerating skin wound healing. Adv Funct Mater. 2024;34:2312374.
13. Gong Y, Wang P, Cao R, Wu J, Ji H, Wang M, Hu C, Huang P, Wang X. Exudate absorbing and antimicrobial hydrogel integrated with multifunctional curcumin-loaded magnesium polyphenol network for facilitating burn wound healing. ACS Nano. 2023;17:22355–70.
14. Chen J, Zhu H, Zhu Y, Zhao C, Wang S, Zheng Y, Xie Z, Jin Y, Song H, Yang L, et al. Injectable self-healing hydrogel with siRNA delivery property for sustained STING silencing and enhanced therapy of intervertebral disc degeneration. Bioact Mater. 2022;9:29–43.
15. Li J, Song J, Deng Z, Yang J, Wang X, Gao B, Zhu Y, Yang M, Long D, Luo X, et al. Robust reactive oxygen species modulator hitchhiking yeast microcapsules for colitis alleviation by trilogically intestinal microenvironment renovation. Bioact Mater. 2024;36:203–20.
16. Liu M, Huang L, Xu X, Wei X, Yang X, Li X, Wang B, Xu Y, Li L, Yang Z. Copper doped carbon dots for addressing bacterial biofilm formation, wound infection, and tooth staining. ACS Nano. 2022;16:9479–97.
17. Zhang H, Lu Y, Huang L, Liu P, Ni J, Yang T, Li Y, Zhong Y, He X, Xia X, Zhou J. Scalable and versatile metal ion solidificated alginate hydrogel for skin wound infection therapy. Adv Healthc Mater. 2024;13: e2303688.
18. Ermini ML, Voliani V. Antimicrobial nano-agents: the copper age. ACS Nano. 2021;15:6008–29.
19. Li Y, Yang L, Liao Y, Zhao R, Ji L, Su R, Xu D, Wang F. Photothermal heating-assisted superior antibacterial and antibiofilm activity of high-entropy-alloy nanoparticles. Adv Funct Mater. 2023;33:2302712.
20. Wen M, Wang T, Li N, Wu Y, Zhang L, Xue Y, Shang L. Polyphenol-copper derived self-cascade nanozyme hydrogel in boosting oxygenation and robust revascularization for tissue regeneration. Adv Funct Mater. 2024;34:2403634.
21. Chen L, Min J, Wang F. Copper homeostasis and cuproptosis in health and disease. Signal Transduct Target Ther. 2022;7:378.
22. Zhang QY, Tan J, Huang K, Nie R, Feng ZY, Zou CY, Li QJ, Chen J, Sheng N, Qin BQ, et al. Polyphenolic-modified cellulose acetate membrane for bone regeneration through immunomodulation. Carbohydr Polym. 2023;305: 120546.
23. Yan JH, Liang CX, Ma RR, Li BJ, Chen QW, Li W, Zeng X, Zhang XZ. Sulfasalazine-loaded copper-tannic acid coordination nanozyme enables ROS scavenging and immunomodulation for inflammatory bowel disease therapy. Adv Healthc Mater. 2024:e2403738.
24. Hou Q, He X, Guo M, Li X, Zhang Z, Xu X, Xu Y, Shi Q, Han Y. Enhanced hemostatic efficacy of cryogel with copper ion-loaded mesoporous bioactive glasses for acute and persistent bleeding. J Nanobiotechnol. 2025;23:102.
25. Kurian AG, Singh RK, Patel KD, Lee JH, Kim HW. Multifunctional GelMA platforms with nanomaterials for advanced tissue therapeutics. Bioact Mater. 2022;8:267–95.
26. Cheng F, Wang S, Zheng H, Shen H, Zhou L, Yang Z, Li Q, Zhang Q, Zhang H. Ceria nanoenzyme-based hydrogel with antiglycative and antioxidative performance for infected diabetic wound healing. Small Methods. 2022;6: e2200949.
27. Li X, Han Z, Wang T, Ma C, Li H, Lei H, Yang Y, Wang Y, Pei Z, Liu Z, et al. Cerium oxide nanoparticles with antioxidative neurorestoration for ischemic stroke. Biomaterials. 2022;291: 121904.
28. Weng Q, Sun H, Fang C, Xia F, Liao H, Lee J, Wang J, Xie A, Ren J, Guo X, et al. Catalytic activity tunable ceria nanoparticles prevent chemotherapy-induced acute kidney injury without interference with chemotherapeutics. Nat Commun. 2021;12:1436.
29. Wu Y, Zhang Y, Tang X, Ye S, Shao J, Tu L, Pan J, Chen L, Liang G, Yin L. Synergistic anti-oxidant and anti-inflammatory effects of ceria/resatorvid co-decorated nanoparticles for acute lung injury therapy. J Nanobiotechnol. 2023;21:502.
30. Wang Y, Li C, Wan Y, Qi M, Chen Q, Sun Y, Sun X, Fang J, Fu L, Xu L, et al. Quercetin-loaded ceria nanocomposite potentiate dual-directional immunoregulation *via* macrophage polarization against periodontal inflammation. Small. 2021;17: e2101505.
31. Liang Y, Li Z, Huang Y, Yu R, Guo B. Dual-dynamic-bond cross-linked antibacterial adhesive hydrogel sealants with on-demand removability for post-wound-closure and infected wound healing. ACS Nano. 2021;15:7078–93.
32. Huang Y, Zhang M, Jin M, Ma T, Guo J, Zhai X, Du Y. Recent advances on cerium oxide-based biomaterials: toward the next generation of intelligent theranostics platforms. Adv Healthc Mater. 2023;12: e2300748.
33. Wu H, Li F, Wang S, Lu J, Li J, Du Y, Sun X, Chen X, Gao J, Ling D. Ceria nanocrystals decorated mesoporous silica nanoparticle based ROS-scavenging tissue adhesive for highly efficient regenerative wound healing. Biomaterials. 2018;151:66–77.
34. Wahba SM, Darwish AS, Kamal SM. Ceria-containing uncoated and coated hydroxyapatite-based galantamine nanocomposites for formidable treatment of Alzheimer's disease in ovariectomized albino-rat model. Mater Sci Eng C Mater Biol Appl. 2016;65:151–63.
35. Joorabloo A, Liu T. Recent advances in reactive oxygen species scavenging nanomaterials for wound healing. Exploration (Beijing). 2024;4:20230066.
36. Jiang C, Shi Q, Yang J, Ren H, Zhang L, Chen S, Si J, Liu Y, Sha D, Xu B, Ni J. Ceria nanozyme coordination with curcumin for treatment of sepsis-induced cardiac injury by inhibiting ferroptosis and inflammation. J Adv Res. 2024;63:159–70.
37. Li L, Zhang C, Cao Z, Ma L, Liu C, Lan X, Qu C, Fu P, Luo R, Wang Y. Passivation protein-adhesion platform promoting stent reendothelialization using two-electron-assisted oxidation of polyphenols. Biomaterials. 2024;305: 122423.
38. Haghniaz R, Montazerian H, Rabbani A, Baidya A, Usui B, Zhu Y, Tavafoghi M, Wahid F, Kim HJ, Sheikhi A, Khademhosseini A. Injectable, antibacterial, and hemostatic tissue sealant hydrogels. Adv Healthc Mater. 2023;12: e2301551.
39. Li Y, Yang Z, Sun Q, Xu R, Li R, Wu D, Huang R, Wang F, Li Y. Biocompatible cryogel with good breathability, exudate management, antibacterial and immunomodulatory properties for infected diabetic wound healing. Adv Sci. 2023;10: e2304243.
40. Li X, Gao P, Tan J, Xiong K, Maitz MF, Pan C, Wu H, Chen Y, Yang Z, Huang N. Assembly of metal-phenolic/catecholamine networks for synergistically anti-inflammatory, antimicrobial, and anticoagulant coatings. ACS Appl Mater Interfaces. 2018;10:40844–53.
41. Yuan T, Yang T, Chen H, Fu D, Hu Y, Wang J, Yuan Q, Yu H, Xu W, Xie X. New insights into oxidative stress and inflammation during diabetes mellitus-accelerated atherosclerosis. Redox Biol. 2019;20:247–60.

42. Zhang Q, Liu J, Duan H, Li R, Peng W, Wu C. Activation of Nrf2/HO-1 signaling: an important molecular mechanism of herbal medicine in the treatment of atherosclerosis *via* the protection of vascular endothelial cells from oxidative stress. J Adv Res. 2021;34:43–63.
43. Li Z, Xing X, Zhao C, Wu Q, Liu J, Qiu X, Wang L. A rapid interactive chitosan-based medium with antioxidant and pro-vascularization properties for infected burn wound healing. Carbohydr Polym. 2024;333: 121991.
44. Yu S, Du J, Zhang Q, Li Z, Ge S, Ma B. Mitochondria-targeted polyphenol-cysteine nanoparticles regulating AMPK-mediated mitochondrial homeostasis for enhanced bone regeneration. Adv Funct Mater. 2024;34:2402463.
45. Kim JE, Yim D, Lee CH, Jun B, Nam J, Han SH, Lee SU, Kim J-H, Kim JW. Environmental stimuli-irresponsive long-term radical scavenging of 2D transition metal dichalcogenides through defect-mediated hydrogen atom transfer in aqueous media. Adv Funct Mater. 2018;28:1802737.
46. Xu J, Chang L, Xiong Y, Peng Q. Chitosan-based hydrogels as antibacterial/antioxidant/anti-Inflammation multifunctional dressings for chronic wound healing. Adv Healthc Mater. 2024; n/a:2401490.
47. Feng Q, Zhang X, Zhao X, Liu J, Wang Q, Yao Y, Xiao H, Zhu Y, Zhang W, Wang L. Intranasal delivery of pure nanodrug loaded liposomes for Alzheimer's disease treatment by efficiently regulating microglial polarization. Small. 2024;20: e2405781.
48. Ashrafizadeh M, Rafiei H, Mohammadinejad R, Afshar EG, Farkhondeh T, Samarghandian S. Potential therapeutic effects of curcumin mediated by JAK/STAT signaling pathway: a review. Phytother Res. 2020;34:1745–60.
49. Kan T, Tian Z, Sun L, Kong W, Yan R, Yu Z, Tian QW, Liu C. Quercetin-loaded zeolitic imidazolate framework-8 (ZIF-8) nanoparticles attenuate osteoarthritis by activating autophagy *via* the Pi3k/Akt signaling. ACS Appl Mater Interfaces. 2024;16:40444–54.
50. Wu Z, Huang S, Li T, Li N, Han D, Zhang B, Xu ZZ, Zhang S, Pang J, Wang S, et al. Gut microbiota from green tea polyphenol-dosed mice improves intestinal epithelial homeostasis and ameliorates experimental colitis. Microbiome. 2021;9:184.
51. Niu C, Chen Z, Kim KT, Sun J, Xue M, Chen G, Li S, Shen Y, Zhu Z, Wang X, et al. Metformin alleviates hyperglycemia-induced endothelial impairment by downregulating autophagy *via* the Hedgehog pathway. Autophagy. 2019;15:843–70.
52. Tang Y, Yu Z, Lu X, Fan Q, Huang W. Overcoming vascular barriers to improve the theranostic outcomes of nanomedicines. Adv Sci. 2022;9: e2103148.
53. Das A, Ash D, Fouda AY, Sudhahar V, Kim YM, Hou Y, Hudson FZ, Stansfield BK, Caldwell RB, McMenamin M, et al. Cysteine oxidation of copper transporter CTR1 drives VEGFR2 signalling and angiogenesis. Nat Cell Biol. 2022;24:35–50.
54. Montanari E, Mancini P, Galli F, Varani M, Santino I, Coviello T, Mosca L, Matricardi P, Rancan F, Di Meo C. Biodistribution and intracellular localization of hyaluronan and its nanogels. A strategy to target intracellular *S. aureus* in persistent skin infections. J Control Release. 2020;326:1–12.
55. Voisin B, Nadella V, Doebel T, Goel S, Sakamoto K, Ayush O, Jo JH, Kelly MC, Kobayashi T, Jiang JX, et al. Macrophage-mediated extracellular matrix remodeling controls host Staphylococcus aureus susceptibility in the skin. Immunity. 2023;56:1561-1577.e1569.
56. Bai AD, Lo CKL, Komorowski AS, Suresh M, Guo K, Garg A, Tandon P, Senecal J, Del Corpo O, Stefanova I, et al. Staphylococcus aureus bacteraemia mortality: a systematic review and meta-analysis. Clin Microbiol Infect. 2022;28:1076–84.
57. Zhang H, Wu J, Lyu Z, Ling J. Impact of alanyl-tRNA synthetase editing deficiency in yeast. Nucleic Acids Res. 2021;49:9953–64.
58. Harris A, Wagner M, Du D, Raschka S, Nentwig LM, Gohlke H, Smits SHJ, Luisi BF, Schmitt L. Structure and efflux mechanism of the yeast pleiotropic drug resistance transporter Pdr5. Nat Commun. 2021;12:5254.
59. Zhang S, Ding F, Liu Y, Ren X. Glucose-responsive biomimetic nanoreactor in bacterial cellulose hydrogel for antibacterial and hemostatic therapies. Carbohydr Polym. 2022;292: 119615.
60. Kazemi N, Javad Mahalati M, Kaviani Y, Al-Musawi MH, Varshosaz J, SoleymaniEil Bakhtiari S, Tavakoli M, Alizadeh M, Sharifianjazi F, Salehi S, et al. Core-shell nanofibers containing L-arginine stimulates angiogenesis and full thickness dermal wound repair. Int J Pharm. 2024;653:123931.
61. Firuzeh M, Labbaf S, Enayati MH, Dinari M, Mirhaj M. Enhanced wound healing with a bilayered multifunctional quaternized chitosan-dextran-curcumin construct. Carbohydr Polym. 2025;352: 123195.
62. Tavakoli M, Al-Musawi MH, Kalali A, Shekarchizadeh A, Kaviani Y, Mansouri A, Nasiri-Harchegani S, Kharazi AZ, Sharifianjazi F, Sattar M, et al. Platelet rich fibrin and simvastatin-loaded pectin-based 3D printed-electrospun bilayer scaffold for skin tissue regeneration. Int J Biol Macromol. 2024;265: 130954.
63. Almajidi YQ, Muslim RK, Issa AA, Al-Musawi MH, Shahriari-Khalaji M, Mirhaj M. Three-dimensional printed polyelectrolyte construct containing mupirocin-loaded quaternized chitosan nanoparticles for skin repair. Int J Biol Macromol. 2024;280: 136214.
64. Zhang W, Wu W, Wang T, Wu Z, Li Y, Ding T, Fang Z, Tian D, He X, Huang F. Novel supramolecular hydrogel for infected diabetic foot ulcer treatment. Adv Healthc Mater. 2024;13:2402092.
65. Dai F, Zhang J, Chen F, Chen X, Lee CJ, Liang H, Zhao L, Tan H. A multi-responsive hydrogel combined with mild heat stimulation promotes diabetic wound healing by regulating inflammatory and enhancing angiogenesis. Adv Sci. 2024;11:2408783.
66. Liang X, Ding L, Ma J, Li J, Cao L, Liu H, Teng M, Li Z, Peng Y, Chen H, et al. Enhanced mechanical strength and sustained drug release in carrier-free silver-coordinated anthraquinone natural antibacterial anti-inflammatory hydrogel for infectious wound healing. Adv Healthc Mater. 2024;13: e2400841.
67. Yan N, Wang Y, Wong TY, Wu Z, Wang X, Xie M, Parodi A, Wang WX, Shi J. Spatiotemporal mapping of the evolution of silver nanoparticles in living cells. ACS Nano. 2024;18:35013–28.
68. Vempati P, Popel AS, Mac GF. Extracellular regulation of VEGF: isoforms, proteolysis, and vascular patterning. Cytokine Growth F R. 2014;25:1–19.
69. Liu N, Zhu S, Deng Y, Xie M, Zhao M, Sun T, Yu C, Zhong Y, Guo R, Cheng K, et al. Construction of multifunctional hydrogel with metal-polyphenol capsules for infected full-thickness skin wound healing. Bioact Mater. 2023;24:69–80.
70. Li Y, Xu T, Tu Z, Dai W, Xue Y, Tang C, Gao W, Mao C, Lei B, Lin C. Bioactive antibacterial silica-based nanocomposites hydrogel scaffolds with high angiogenesis for promoting diabetic wound healing and skin repair. Theranostics. 2020;10:4929–43.

Publisher's Note